Engineered Science
DOI: https://dx.doi.org/10.30919/es8d851

# Chitosan-based Magnetic Particles as Adsorbents for Anionic Contaminants

Melina Kloster,[1] Adriele A. de Almeida, [2] Diego Muraca,[2] Norma E. Marcovich[1] and Mirna A. Mosiewicki[1,*]

## Abstract

An environmentally friendly nano-sized adsorbent with good adsorption capacity for ionic contaminants, that can be easily removed from treated water, was obtained. The adsorbent consists in iron oxide magnetic nanoparticles coated with chitosan, resulting in a core-shell structure. The particles were obtained by a two-step procedure that includes the synthesis of the magnetic core nanoparticles by the alkaline co-precipitation method, followed by their immersion in a dilute chitosan solution. They were characterized and the presence of the organic coating was verified using different techniques. The adsorbent properties were studied using Congo red (CR) solutions, as an example of common ionic adsorbates discharged into the waste streams by textile industries. Adsorption kinetics studies at different CR concentrations and adsorption equilibrium isotherms at two pHs are reported and modeled theoretically. The pseudo-second-order model was the one that best fitted the adsorption kinetics and for equilibrium studies, the best fit was with either the Langmuir model (pH 7) or the Freundlich model (pH 3). The dye adsorption at lower pH was higher than that exhibited by neutral solutions, attributed to the increase in electrostatic attraction between the negatively charged dye molecule and positively charged amine group of chitosan. Preliminary results for CR desorption are also reported.

*Keywords:* Magnetic nanocomposite particles; Chitosan; Core-shell structures; Adsorption properties.
Received: 16 December 2022; Revised: 13 March 2023; Accepted: 22 March 2023.
Article type: Research article.

## 1. Introduction

Environment contamination, particularly pollution of water with heavy metals and other ionic compounds is an issue that affects many ecosystems and communities all around the world. Contamination of water sources and water scarcity are increasing by factors like population explosion, urbanization, rapid industrialization, and various other harmful anthropogenic activities. The wastewater may be contaminated with various inorganic as well as organic pollutants such as dyes,[1-3] products from pharmaceutical industries,[4] pesticides, personal care products (PCP),[5] chemicals that may affect the endocrine process of organisms, surfactants, toxic metals, *etc*.[6]

Synthetic dyes are considered unpleasant and dangerous organic compounds for the environment. They are problematic as they are toxic and non-biodegradable because of their complex and stable structures, so the removal of dyes from waste water has become a great challenge for all scientists in the world.[7] Even so, they are widely used in diverse applications including textiles, pharmaceuticals, food and beverages, paper manufacturing, leather, and so on, to impart color to various substrates.[8,9] It is estimated that >100,000 kinds of dyes are circulating in the market with an annual worldwide production of over $7 \times 10^5$ tons.[8,10,11] The global textile industry is one of the major contributors to aquatic pollution across the world.[10] It is one of the heavily water-dependent industries requiring almost 200-270 tons of water for producing one ton of textile product, with a global water requirement of about 79 billion cubic meters of water annually.[10,12] The majority of the textile sector globally is also quite inefficient, leading to almost $2 \times 10^5$ tons of synthetic dyes being discharged into the environment. The World Bank also estimates the contribution of industrial wastewater from

---

[1] *Instituto de Investigaciones en Ciencia y Tecnología de Materiales (INTEMA), Facultad de Ingeniería, Universidad Nacional de Mar del Plata – CONICET, Mar del Plata 7600, Argentina.*
[2] *Instituto de Física Gleb Wataghin (IFGW), Universidade Estadual de Campinas – UNICAMP, Campinas, São Paulo 13083-859, Brazil.*
**Email:* mirna@fi.mdp.edu.ar (M. A. Mosiewicki)

textile dyeing and finishing treatment by about 17–20 % worldwide.[13] The presence of dye materials even in small quantities greatly influences the visibility, appearance, and quality of water, which is esthetically nasty.[14] Additionally, most dyes are toxic, mutagenic, and carcinogenic in nature.[15] In particular, Congo Red is one of the most widely used anionic dyes in the textile industry, whose removal from wastewater is crucial because it can be metabolized to benzidine, a known human carcinogen.[16]

Owing to their complicated chemical structures, dyes are difficult to treat with municipal waste treatment operations[17] and conventional processes for the treatment of metal-bearing effluents generally face economic or environmental constraints that make them ineffective for removing toxic or strategic metal ions at low or trace levels from aqueous waste streams.[18] In this way, the elimination and subsequent recovery of contaminants from wastewater require the development and implementation of new technologies. Among the options, adsorption is one of the most adequate techniques for purification purposes because of its simplicity, low cost, high efficiency, adsorbent disponibility, *etc*.[19] Compared to conventional micron-sized supports used in the separation process, nanometric sorbents have quite good performance due to their high specific surface areas and the absence of internal diffusion resistance. However, nano-adsorbents face serious drawbacks in terms of separation and recovery from treated solutions: they usually require sophisticated separation processes, such as very fine filtration or centrifugation. In this line, magnetic nano-adsorbents offer interesting alternatives for phase separation using an external magnetic field for the recovery of spent sorbents[18] while reducing the chance of any secondary pollution.[20]

Among iron oxides, maghemite, and magnetite[21] present ferromagnetic behavior. However, magnetite is generally preferable for magnetic separation applications.[22]

Magnetite nanoparticles with their functionalized surface have received increased interest due to their potential applications. The unavoidable problems of naked iron oxide nanoparticles, such as agglomeration and oxidization by air due to their high chemical activity, limit their application since would cause damage to magnetic properties.[23,24] To provide the magnetite nanoparticles with higher resistance to highly acidic aqueous media and to prevent their oxidation, degradation, and dissolution, it is possible to coat them with chemically resistant organic or inorganic layers, resulting in core-shell structures.[18] Surface modification of magnetite nanoparticles could include organic compounds that would provide similar functionality to common extractants for anionic or cationic species.[25] Thus, these functionalized nanoparticles could be used as more specific and highly effective adsorbent nanomaterials.[22] In fact, the adsorption of dyes by means of natural and biodegradable polymers is one of the emerging methods for dye removal[26] because of their inherent adsorption properties, but also due to their green nature.

Chitosan (Ch) is a biodegradable, biocompatible, hydrophilic, and non-toxic natural polymer that is obtained from partial or total chitin deacetylation. Chitin is the main component of the crustacean exo skeleton and the second most abundant biopolymer present in nature. As chitosan has excellent properties for adsorption and encapsulation due to amino groups (-$NH_2$) present in its backbone that act like reaction and coordination sites, its ideal to be used as a polymeric coating for adsorption purposes.

The adsorption of Congo red has been studied using adsorbents based on chitosan, iron oxide nanoparticles, composite materials/particles based on both (as presented in this work), or even more complex ones. Among these, it is worth mentioning the works of Jeyaseelan *et al*.[27] that studied the use of sulfate-cross-linked chitosan particles, that of Feng *et al*.[28] that developed cross-linked porous chitosan films, the one of Ohemeng-Boahen *et al*.[29] that synthesized chitosan/hematite nano-composite hydrogel capsules intended as CR adsorbents, that of Kloster *et al*.[30] that manufactured chitosan-magnetite composite films, *etc*. Also, more recently, Zhang *et al*.[31] developed chitosan–vanadium-titanium-magnetite composite adsorbent, Chatterjee *et al*.[32] manufactured goethite-impregnated chitosan hydrogel capsules while Tan *et al*.[33] fabricated ethylenediamine-functionalized magnetic microspheres with large mesopores, Zong *et al*.[34] synthesized a magnetically recyclable $Mg(OH)_2/Fe_3O_4$/PEI functionalized enzymatic lignin composite bio-adsorbent, Wang *et al*.[35] developed a magnetic adsorbent from chitosan and $Fe_3O_4$ by a solvent-free ball milling method, Sarojini *et al*.[36] manufactured polypyrrole-iron oxide-seaweed nanocomposites, and Huang *et al*.[37] synthesized in situ quaternary-ammonium-functionalized magnetic chitosan microspheres.

In this work, nanosized adsorbents consisting of a magnetic iron oxide core coated with a shell of chitosan biopolymer were prepared by a simple procedure and systematically characterized by means of XRD, FTIR, TGA, TEM, DLS, XPS, and magnetic analysis. Congo red was further used as a model dye to evaluate its adsorption and desorption properties.

## 2. Experimental procedures

### 2.1 Materials

Chitosan in powder form (degree of deacetylation 98%, Mv = 1.61 × $10^5$ g $mol^{-1}$) was supplied by Parafarm. The ferric chloride hexahydrate ($FeCl_3$-$6H_2O$), ammonium hydroxide (25% $NH_3$), sulfuric acid, and sodium hydroxide were obtained from Sigma-Aldrich. Glacial acetic acid and the ferrous chloride tetrahydrate ($FeCl_2.4H_2O$) were obtained from Biopack. All these reagents were analytical grade and were used without further purification.

Congo red (CR) dye (Solarbio®) of analytical grade without further purification was used as adsorbate. Congo red is an anionic diazo direct dye (CR, CI 22120, molecular weight 696.7 g $mol^{-1}$) that contains $NH_2$ and $SO_3^-$ functional groups.

## 2.2 Methods

### 2.2.1 Synthesis of core-shell magnetic nanoparticles (NP-Ch)

The iron oxide nanoparticles (NPs) were obtained by an alkaline co-precipitation method adapted from that developed by Massart and Cabuil[38] and previously reported by Kloster *et. al.*[39]. Aqueous solutions of ferric chloride ($FeCl_3.6H_2O$) and ferrous chloride ($FeCl_2.4H_2O$) were prepared and mixed by magnetic stirring using a molar ratio $Fe^{+2}$:$Fe^{+3}$ = 2:1. Once the solution was completely homogenized, concentrated $NH_4OH$ (25-30%) solution was added to promote the magnetic NPs precipitation. During this step, the suspension was manually stirred for 5 minutes, by means of a glass rod. Then, the particles were separated by magnetic decantation and washed several times with deionized water until neutral pH. Finally, NPs were redispersed in deionized water in a mass ratio NP: $H_2O$ = 0.032 and stored until further use.

To prepare the core-shell adsorbent particles, an aqueous suspension containing 1 g of iron oxide nanoparticles was mixed with 100 mL of chitosan solution (2 % w/v) prepared by dissolving chitosan powder in aqueous acetic acid solution (1% v/v) by magnetic stirring at room temperature. This dispersion was submitted to orbital shaking at 250 rpm for 1 h at room temperature. The obtained coated iron oxide nanoparticles (NP-Ch) were washed with deionized water several times and separated from the supernatant liquid by centrifugation (12500 rpm for 15 minutes), until neutral pH. This synthesis procedure is summarized in Scheme 1. The final suspensions were kept in dark-colored glass containers for further use.

### 2.2.2 Characterization of NP-Ch

### X-ray diffraction (XRD)

The crystal structure of the nanoparticles was investigated using CuKα radiation (λ=1.5418 A) in a PANalytical X'Pert Pro diffractometer operated at 40 kV, 300 mA, and 0.6 °C $min^{-1}$. The average crystal grain sizes were calculated from the Scherrer Equation (1) with XRD line broadening, assuming crystals are spherical:

$$\tau = \frac{0.9\,\lambda}{\beta\, Cos\,\theta} \tag{1}$$

where, τ the mean size of the ordered (crystalline) domains, λ the wavelength of the X-ray, θ the diffraction angle in degrees, and β, in radians, the measured full width at half maximum intensity. The diffraction peak at 2θ = 35.4°, which corresponds to the lattice plane (3 1 1), was used for calculation since it is well resolved and shows no interferences.

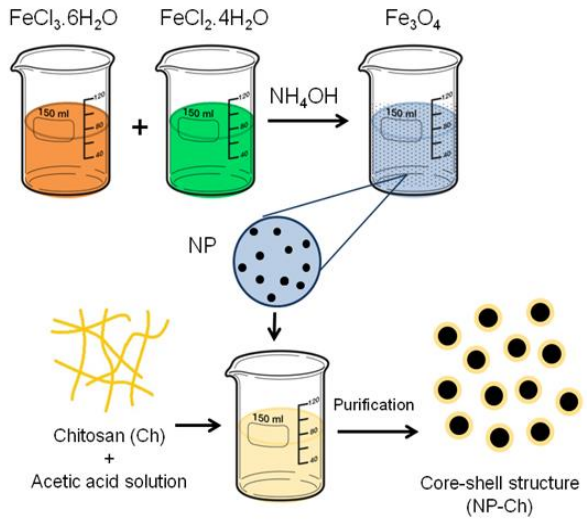

**Scheme 1** Schematic representation of the synthesis of the core-shell magnetic nanoparticles.

### Transmission Electron Microscopy (TEM)

TEM analysis was performed on a JEOL JEM 2100, 200KV, and $B_6La$ filament field-emission gun transmission electron microscope (voltage: 200 kV). Particle suspensions were dried by lyophilization and then, a small number of nanoparticles were dispersed in isopropyl alcohol. Samples for the microscopy experiment were then prepared by drying a drop of this suspension on a Ted Pella ultrathin cooper film on a holey carbon.

### Infrared spectroscopy (FTIR)

FTIR spectra of chitosan powder and nanoparticles with and without coating were recorded in transmission mode (samples included in KBr pellets), using a Thermo Scientific Nicolet 6700 spectrometer. The spectra were recorded over a range of 500–4000 $cm^{-1}$ with a resolution of 2 $cm^{-1}$ and averaged over 32 scans.

### Thermogravimetric analysis (TGA)

Thermogravimetric tests of the iron oxides nanoparticles with and without coating were performed in a TGA-40 Shimadzu Thermogravimetric Analyzer at a heating rate of 10 °C min$^{-1}$ under air atmosphere (35 mL min$^{-1}$) from room temperature to 900 °C.

### X-ray photoelectron spectroscopy

X-ray photoelectron spectroscopy (XPS) chemical state analysis was performed in a Thermo Scientific, K-Alpha X-ray Photoelectron Spectrometer that includes a hemispheric analyzer with the double focus of 180°, a 128 channel detector, and an EX06 ion source, using Al Kα excitation with variable point size (from 30 to 400 μm in increases of 5 μm).

### Magnetic characterization

The magnetic properties of NPs with and without chitosan coating were obtained using a commercial SQUID magnetometer (Quantum Design, MPMS®3). In this way, both isothermal magnetization curves (M(H)) as well as magnetization measurements as a function of temperature (M(T)) were performed in order to characterize the magnetic properties of the NPs. M(H) curves were performed at two different temperatures, 2K and 300K. M(T) curves were measured with an applied field of 50 Oe in zero field cooling (ZFC) and field cooling (FC) protocols. For the ZFC protocol, the sample was first cooled down from T = 300 to 2 K in zero magnetic fields, then a static magnetic field of 50 Oe was applied and the magnetization was measured while increasing the temperature up to 350 K. Subsequently the sample was cooled down to 2 K under the same applied magnetic field (50 Oe) and the magnetization was measured while warming up the sample from 2 K to 350 K. The average value of the blocking temperature distribution function ( $f(T_B)$ ) was calculated from the FC/ZFC curves using the derivative expression d(FC-ZFC)/dT and used in $< T_B >= \frac{\sum T * f(T_B)}{\sum T}$.

M(H) measurements at 300 K were used to determine saturation magnetization ($M_S$) at room temperature and to estimate the magnetic volume by modeling the magnetization by fitting the curves with the Langevin function, considering monodomain magnetic NPs with small dipolar interaction among them and near the superparamagnetic behavior.[40]

For these measurements, the magnetic NPs were dispersed in epoxy resin at low concentrations (i.e. sample NP: 0.3 wt.%, sample NP-Ch: 0.01 wt.% and sample NP-Ch-CR: 0.2 wt.%, in order to avoid agglomeration and physical rotation of the NPs with the applied field).

Two repetitions of each of the characterization procedures presented in this section were carried out since the measurements gave the same results in both cases.

### Dynamic light scattering

The average particle size and particle size distribution of the nanoparticle dispersions were measured by dynamic light scattering (DLS) using a Malvern Zetasizer Nano S90 with a laser beam 42 of 632 nm (Malvern Instruments Co. Ltd., Worcestershire, 43 UK) at 25 °C. Very dilute dispersions in distilled water (~ 0.005 mg $_{\text{particles}}$ mL$^{-1}$) were used to get accurate results. Sonication was applied for 30 minutes prior to the measurements to separate micrometric agglomerates formed during storage into smaller ones.

### Colloidal stability

To evaluate the colloidal stability of the nanoparticles, suspensions at neutral and acid pH, containing 0.01 mg$_{\text{particles}}$ mL$^{-1}$, were prepared using distilled water and sulfuric acid to adjust the pH. The flasks containing the suspensions were left at room temperature for 24 h. The absorbancies of the suspensions at λ=420 nm were measured at t=0 and t=24 h using a UV-vis spectrophotometer (Agilent 8453). The results were interpreted according to the suggestions of Xu *et al*.[41]

### 2.2.3 Adsorption and desorption tests

Congo red (CR) solutions with different concentrations were prepared by diluting the dye in Milli-Q water. Since Congo red aqueous solutions are red at pH>5 and blue at pH<3,[42] calibration curves were prepared by using a UV-vis spectrophotometer (Agilent 8453), by measuring the absorbance of solutions of different concentrations at λ=498 nm for neutral pH and λ=570 nm for acid pH, where the dye has maximum absorbance.[43,44] Then, for subsequent determinations, the concentration of CR was calculated from the corresponding calibration curve.

Equilibrium and kinetic tests were carried out using 0.1 g of NP-Ch or uncoated NP (only kinetic studies) as adsorbents that were previously lyophilized for 24 h (100 mbar and -60 °C). The nanoparticles were added to flasks containing 20 mL of CR solutions and the whole system was submitted to orbital shaken at 60 rpm at room temperature (25 ± 1°C). For kinetic studies, different contact times were evaluated using CR solutions with initial concentrations of 10 mg L$^{-1}$ and 100 mg L$^{-1}$. For the equilibrium tests, the contact time was 24 h and the CR initial concentration was varied from 50 to 200 mg L$^{-1}$. After each period, the particles were separated from the flasks by magnetic decantation, and the concentration of the remaining CR solutions was measured by UV-vis spectrophotometry. The adsorption capacity of the particles was calculated using Equation 2:

$$q_t = \frac{(C_0 - C_t).V}{W} \tag{2}$$

where $q_t$ represents the adsorption capacity ($\mathrm{mg_{CR}}\ (\mathrm{g_{adsorbent}})^{-1}$) at any time, $V$ is the volume of the solution (L), $W$ is the weight of adsorbent (g) and $C$ is the concentration of CR at the initial ($C_0$) and time t ($C_t$) conditions ($\mathrm{mg_{CR}}\ (\mathrm{L}\ _{\mathrm{solution}})^{-1}$). For equilibrium measurements (isotherms), $C_t$ was replaced by $C_e$ (equilibrium concentration).

Kinetic studies were performed at the natural pH of CR solutions, which was ~6.5-7 but equilibrium isotherms were also evaluated with CR solutions of pH ~3, achieving this condition by adding sulfuric acid 0.1 mol $\mathrm{L^{-1}}$.

Preliminary desorption tests were carried out on the samples used in adsorption tests at pH ~3. The particles were recovered from the treated CR solutions by magnetic separation and subsequently transferred to flasks containing 20 mL of aqueous NaOH solution at pH~13 for 24 h under orbital shaking. After this time, $q$ was calculated as the difference between the initially adsorbed amount of dye and the one that was desorbed to the aqueous phase.

Two replicates of most of the samples were used in the adsorption tests. In these cases, the average error in the measurements was below 10%.

## 3. Results and discussion

### 3.1 X-ray diffraction (XRD) analysis

Figure 1 shows the XRD patterns of NP and NP-Ch obtained by XRD. In both spectra, the positions and relative intensities of the diffraction peaks (2θ = 30.1°, 35.5°, 43.3°, 53.4°, 57.2° and 62.7° that can be attributed to (2 2 0), (3 1 1), (4 0 0), (4 2 2), (5 1 1) and (4 4 0) planes, respectively), match with a face-centered cubic (FCC) with inverse spinel structure that corresponds to standard magnetite ($Fe_3O_4$) crystals (standard XRD database JCPDS No. 19–0629) and/or to its polymorphous maghemite ($Fe_2O_3$).[45-47]

However, it is clear that the presence of chitosan coating, expected as a wide band overlapped to the NP diffractogram and centered at ~ 23°, which would correspond to the amorphous structure of the natural polymer,[48] and peaks at 2θ = 9° and 12°, attributed to crystalline hydrated chitosan structure, cannot be observed in the NP-Ch diffractogram, although the very small peaks at 2θ = 18.5°, 20.7° and 30.5° (shoulder) that could be related to the weak crystallinity of chitosan[49] are noticeable, even though with very little intensity. We believe that this is due to the low mass of biopolymer incorporated, in addition to the large intensity of iron oxide peaks that mask the chitosan contribution in the NP-Ch XRD pattern. Similar results were found in other works[20,49-51] in which the researchers concluded in that the

magnetite structure, *e.g.* polymer chain embedment in oxide, contributing to lower the size of coherently diffracting

chemical conjugation of chitosan did not lead to any phase changes of the NP.

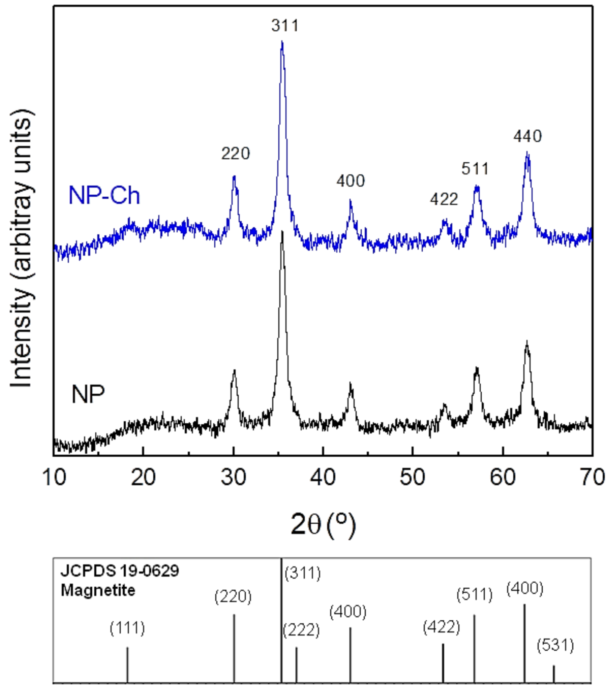

**Fig. 1** X-ray diffraction patterns of NP, NP-Ch, and the standard diffraction pattern for magnetite (JCPDS no. 19-0629).

As characteristic peaks of NP-Ch are slightly shifted to lower angles, an inter-planar distance of (3 1 1) results smaller (2.5305 Å) in NP-Ch than that (2.5344 Å) of naked NP. However, these differences are not significant enough to associate them with more compact particles.

The width at half maximum of the major peak increases slightly after capping, as noticed in related works.[52] In addition, the characteristic peaks of NP-Ch are slightly shifted to lower angles in comparison with the spectra of naked NP. Therefore, the crystallite size decreases after the surface coating, and the values obtained from the Scherrer equation were 9.93 nm and 9.61 nm, for NP and NP-Ch, respectively.

These results could be ascribed to chitosan acting as a controller of the crystallite size that can be associated with the Fe-chitosan complex formed just on the surface of the particles, since in the present work neat NP is first synthesized and then coated with the bio-polymer. During the coating step of the magnetic core with chitosan, the binding of the biopolymer by physical and/or chemical interactions can cause distortion in the crystalline character of the particle surface, consequently reducing the crystallite size that can be determined by measurements in XRD. According to Robinson *et al.*, coating magnetite nanoparticles with starch could induce defaults in domains.[53]

According to Freire *et al.*,[54] when the Fe-chitosan complex is formed prior to the nucleation of the particles, it positively interferes in the crystal growth process by controlling the iron ions diffusion, leading to the formation of crystals with a narrow size distribution and small diameter. Moreover, a reduction in crystallite size was also observed by Antarnusa *et al.*,[55] for iron oxide nanoparticles coated with polyethylene glycol (PEG) synthesized by a two-step procedure similar to the used in this work; which was attributed to the influence of PEG that reacted and functioned as an agent that could limit crystal growth.

Figure 2 shows representative transmission electron micrographs of the synthesized iron oxide NP (Fig. 2a) and NP-Ch (Fig. 2c) as well as the size distributions obtained by counting more than 100 particles from selected images taken at high magnification (Figs. 2b and 2d, respectively).

From the analysis of the histograms, average particle diameters of 8.4 ± 0.3 nm and 8.6 ± 0.3 nm for NP and NP-Ch, respectively, with narrow size distributions, were calculated (dashed line represents the best fit according to a lognormal size distribution).

The smallness in the mean sizes calculated from the TEM micrographs of samples (especially when compared to the respective crystallite sizes) is attributed to the intrinsic characteristics of the transmission microscopy measurements that could consider part of the sample instead of the whole because the observed particles are only those that remained in the grid after the various washing steps performed on the very dilute suspension deposit. Additionally, the two-step preparation procedure involves first the preparation of the magnetic cores and then their redispersion in deionized water and storage until further mixing with the chitosan solution, which could lead to the larger magnetic particles remaining at the bottom of the redispersion container where the suspension was stored, not being transferred to the flask containing the chitosan solution thus resulting in NP and NP-Ch having almost the same average diameter (no significant differences), at least when determined by TEM microscopy.

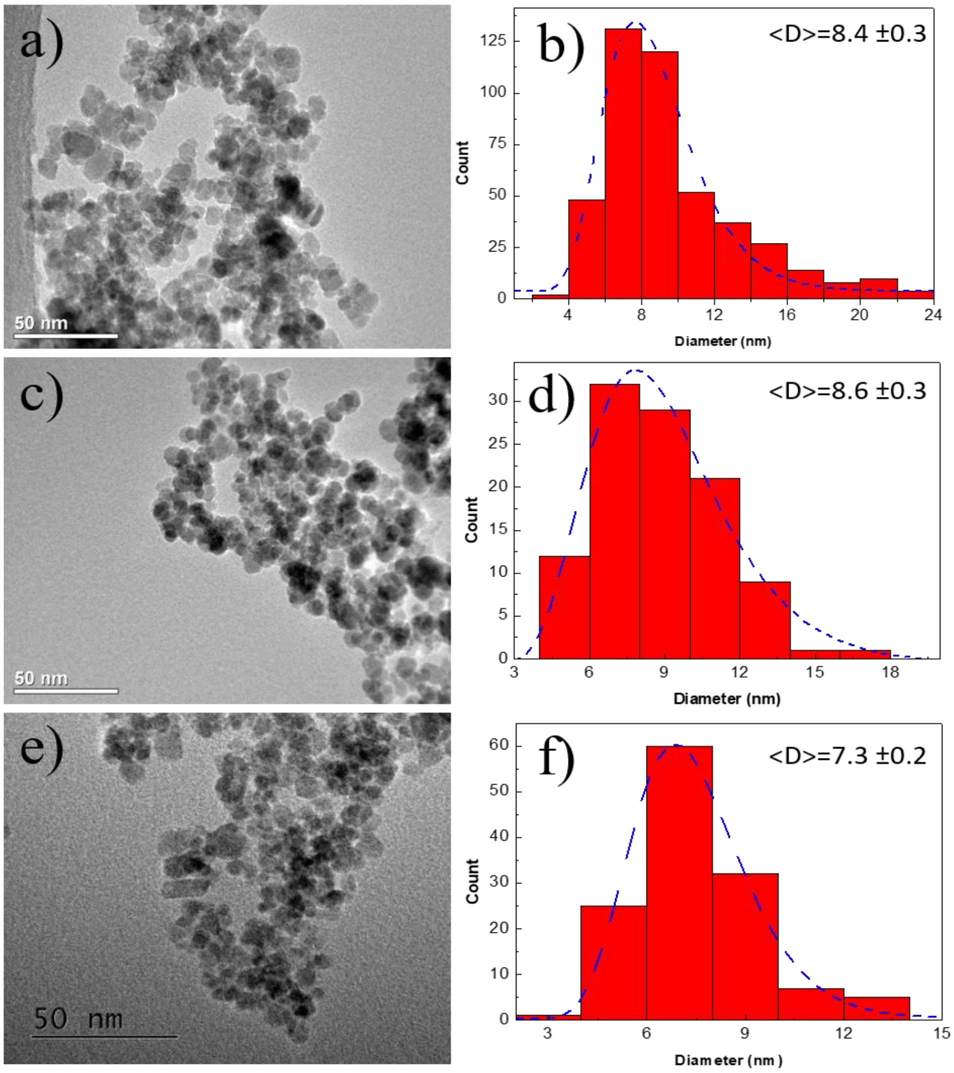

**Fig. 2** TEM images and particle size distributions of uncoated NP (a, b), NP-Ch (c, d) and NP-Ch after adsorption dye process (e, f).

Figure 2 also reveals that NPs seem to be mostly spherical in shape, presenting some agglomeration as can be expected for magnetic NP without surface treatments/surfactant.[23,24,56] The incorporation of a shell of chitosan into the core of magnetic iron oxides does not change the shape of the particles. However, the agglomeration of $Fe_3O_4$ nanoparticles still occurred after encapsulation by chitosan, indicating that particles would have agglomerated in the drying process for preparing the testing sample, as explained in related studies.[57]

Figures 2e and 2f present a TEM image of the nanoparticles recovered from an adsorption test as well as the corresponding histogram. The mean average diameter of the particles is, in this case, 7.3 ± 0.2 nm, the lower value of the series, which can be explained again by considering the loss of the larger particles in the different processing/recovering stages. On the other hand, it is clear that the shape of the particles does not change due to dye adsorption, revealing that the chitosan surface coverage is homogeneous.

### 3.2 Fourier transform infrared (FTIR) analysis

The presence of chitosan in modified NP was also investigated through FTIR; Fig. 3a presents the spectra of chitosan (powder), iron oxide NP and core-shell NP.

In the NP spectrum, the wide absorption band in the rage 700-400 $cm^{-1}$ corresponds to the inorganic lattice vibration and thus, is attributed to the iron oxide ($Fe_3O_4$/$\gamma$-$Fe_2O_3$).[58] This band includes the presence of two strong absorption peaks at around 636 and 592 $cm^{-1}$ corresponding to the formation of magnetic nanoparticles, being the last band confirmed as the Fe-O stretching vibration of tetrahedral sites of spinel structure and an additional absorption band at 459 $cm^{-1}$, attributed to tetrahedral and octahedral sites in the $Fe_3O_4$ structure.[59] The peak at 3423 $cm^{-1}$ is assigned to the stretching vibration of O-H (non-dissociated O-H groups), the peak at 1622 $cm^{-1}$ to the O-H stretching mode, and the peak at 1400 $cm^{-1}$ to the bending vibration of H-O-H due to the water on the particles surface.[49,59,60]

The spectrum of NP-Ch also shows a wide absorption band starting at about 700 $cm^{-1}$, which confirms the presence of iron oxide in the composite particles. It also exhibits a broad band centered on 3420 $cm^{-1}$, which in this case is assigned to -OH hydrogen bonded with the contribution of the $–NH_2$ group-stretching vibration,[61-63] and peaks at 2926 and 2854 $cm^{-1}$ corresponding to stretching vibrations of $CH_2$ and CH (tertiary) aliphatic groups, respectively, attributed to the chitosan coating. The presence of chitosan in the NP-Ch can also be recognized in the band between 1174 and 1040 $cm^{-1}$, due to the stretching vibration of C-O-C links and deformation of C-O and O-H groups from primary and secondary alcohols present in chitosan molecules,[63-66] and in the small peak at 895 $cm^{-1}$ of the β linkage of the glucoside rings (i.e. wagging of the saccharide structure).[63,67] The peaks due to the bending vibrations of methylene and methyl groups at 1375 $cm^{-1}$ (amide III) and 1446 $cm^{-1}$, respectively, and the distinctive absorption band at 1630 $cm^{-1}$ (amide I), are also visible in the spectrum of the core-shell nanoparticles.[59,63]

On the other hand, the spectrum of chitosan powder presents all the expected peaks: the characteristic biosorption peaks of primary amine ($–NH_2$) appear at 3436 (overlapped with that of the O–H stretching vibration) and at 1655 $cm^{-1}$, the band at 1599 $cm^{-1}$ is assigned to N–H bending vibration and the peak of 1378 $cm^{-1}$ to the -C-O stretching of the primary alcoholic group in the polysaccharide. However, these peaks exhibit different relative intensities as compared with those of the NP-Ch and, in some cases, they appear at slightly shifted positions,[20,50,51] confirming that chitosan was successfully coated on $Fe_3O_4$ nanoparticles.

### 3.3 Thermogravimetric analysis (TGA)

The thermogravimetric analysis (TGA) technique provides information on temperature-dependent changes in mass associated with, for example, desorption, decomposition, and sublimation, among others.[22] Fig. 3b shows the thermogravimetric curves (TGA) for NP and NP-Ch in an air atmosphere. Both particles were previously dried in a vacuum oven to constant weight and then kept in a desiccator containing dry silica gel until testing. Despite this, the weight loss curves as a function of the temperature for NP and NP-Ch show a small initial mass loss (~ 1.5 %) below 200 °C, which is attributed to the evaporation of physically adsorbed water, gained during the preparation of the samples for TGA tests, due to the high hydrophilicity of both iron oxide and chitosan. The most important thermal degradation step is observed in the temperature range of 200 to 400 °C and while the $Fe_3O_4$ particles correspond to the escape of the structured water,[68] in the case of the core-shell particles is attributed to the decomposition of the anchored organic polymer due to chemical degradation and deacetylation of chitosan and, at higher temperatures (400 to 600 °C), to oxidative degradation of the carbonaceous residue formed during the previous stage.[68-70] The distinctive TGA curves of the naked $Fe_3O_4$ and $Fe_3O_4$–chitosan nanoparticles, could be used to estimate the content of chitosan coating on the iron oxide nanoparticles. Thus, the relative amount of chitosan in the NP-Ch was determined as 1.85 %, calculated from the residual mass after the degradation of the organic coating. The increase in mass observed in the curves of both samples at high temperatures is because the thermal degradation in the air atmosphere of

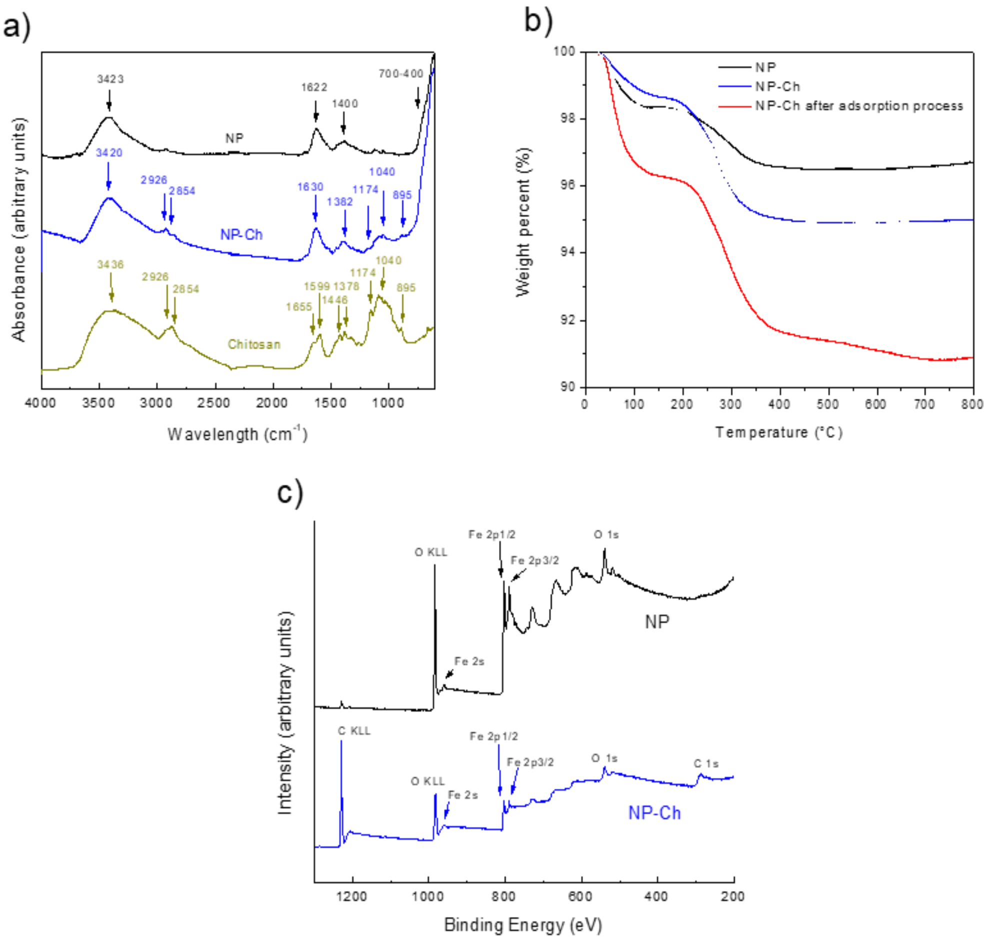

**Fig. 3** a) FTIR spectra of chitosan, uncoated NP, and core-shell NP; b) thermograms of NP and NP-Ch (raw and after CR adsorption process); c) high-resolution XPS spectra of NP and NP-Ch nanoparticles.

magnetite/maghemite leads to oxidation to the oxide of iron (III), $Fe_2O_3$, which was taken into account for the calculation of the amount of biopolymer coating. This means that for the same amount of Fe initially present, the number of oxygen increases due to the oxidation reaction and this is seen reflected in an increase in mass.

Figure 3b also presents the curve of TGA corresponding to NP-Ch exposed to the CR adsorption process, washed with distilled water, and dried before testing. Even when this sample presents a higher amount of initial water (~ 3.8 %) than NP and NP-Ch, it is clear that the nanoparticles after the adsorption process lose more mass (2.1%) than that corresponding to the percentage of the chitosan capping the magnetic core (1.85%), which indicates that CR retained by the particles is also lost during the thermogravimetric analysis test.

### 3.4 X-ray photoelectron spectroscopy

The oxidation states of individual elements and the nature of the intermediate bonding between materials for the neat and chitosan-coated nanoparticles were also studied using X-ray photoelectron spectroscopy (XPS). The obtained survey spectra are shown in Fig. 3c. The full-scale survey spectrum of the NP indicated the presence of iron and oxygen from their characteristic Fe 2s, Fe 2p1/2, Fe 2p3/2, and O 1s peaks, with binding energy values of 962.4, 803.0, 791.0 and 514.2 eV, respectively. On the other hand, the NP-Ch spectrum shows Fe 2s, Fe 2p1/2, Fe 2p3/2, O 1s, and C 1s peaks with binding energy values of 962.1, 801.0, 789.0, 539.1, and 284.1 eV, respectively. Both, the O 1s peak due to the oxygen species and the Fe 2p peaks are present in the spectra of both kinds of nanoparticles, corroborating the obtaining of $Fe_3O_4$-based structures,[71, 72] whereas the C 1s peak corresponding to the C–NH and C–N bonds present in chitosan,[71,72] only appears in the NP-Ch spectrum thus confirming the chitosan coating in these nanoparticles.

### 3.5 Magnetic properties

The magnetic behavior of the core-shell nanoparticles (NP-Ch) was qualitatively evaluated. Fig. 4 shows the performance of the synthesized nanoparticles: they are clearly attracted as a magnet approach, confirming their magnetic character even

**Fig. 4** Magnetic separation of NP-Ch with commercial permanent magnet (NdFeB).

when included in the core-shell structure. Moreover, the magnetic attraction occurs very quickly, which would lead to very short processing times in industrial applications, corroborating that recovery after aqueous remediation treatment can be easily and economically accomplished.

Figure 5 shows the isothermal magnetization curves obtained at 2 and 300 K, in applied field H up to 7 Tesla, as well as the field cooling (FC) and zero field cooling (ZFC) measurements for the magnetic NP, chitosan-coated iron oxide particles (NP-Ch) and NP-Ch with adsorbed CR (NP-Ch-CR). Details of magnetization loops near the coercive field are shown in the inset of each figure. For the magnetization loops (M(H)) at 2 K, the obtained saturation magnetization (Ms) was near ~ 91 emu $g^{-1,}$ and a low value of coercive field ($H_C$) of 250 Oe was observed. At 300 K (room temperature), no hysteresis was observed indicating super-paramagnetic behavior. Moreover, from measurements at 300 K, Ms of 76 emu $g^{-1}$ was obtained, very close in magnitude to that for the bulk $Fe_3O_4$ (Ms ~ 90 emu/g).[73] The difference between bulk and measured Ms can be attributed to surface effects due to particle diameter reduction.[74] Ms of the samples does not change significantly when the magnetic nanoparticles (NPs) go through the process of adding the Ch and the Ch plus the CR adsorption on the surface (Fig. 5). This is an important result for a magnetic adsorbent since variation in Ms can also change the value of the field needed to attract the NPs and consequently, the time in which they are attracted, as Ms and H are directly proportional.

Since no hysteresis (Hc~0) was observed at 300 K, we obtained the magnetic volume from field dependence magnetization using Langevin formalism, resulting in an average magnetic diameter of 7.8 nm, with no significant differences among samples. Fig. 5 (lower left) shows the good agreement between the experimental curve and the theoretical fit obtained for the NP sample, which is representative of the behavior achieved for the other samples. Moreover, these results are in agreement with the diameter obtained from the TEM and confirm that the differences noticed in the latter technique were due to issues associated with the preparation of the sample for TEM tests. Furthermore, the good agreement between “magnetic size” and the size obtained from the TEM images indicates that all samples have almost negligible magnetic interaction and are near the superparamagnetic regime at this temperature, issues that are requirements to avoid large aggregates during later use.

Regarding M(T) (ZFC and FC protocols) measurements, a reversible behavior is observed at room temperature but a progressive blocking of the magnetic moment of the NPs takes place as the temperature decreases (irreversibility), according to the distribution of barrier energies. That is, the magnetic nanoparticles change from the superparamagnetic to the blocked regime as the temperature decreases. The FC magnetization curve of any particle decreases with increasing temperature, a typical response of non-interactive systems, that is, having no magnetic dipole-dipole interactions.[75]

The mean blocking temperatures $<T_B>$ were calculated and found to be near 30 K for all samples (i.e. 34 K for NP, 31 K for NP-Ch, and 32 K for NP-Ch-CR), evidencing that the magnetic characteristics of the different samples do not differ substantially. On the other hand, it is interesting to notice that the NP-Ch sample, despite having a distribution of blocking temperatures quite similar to the others, has a slightly different curve shape and a maximum in the ZFC at a slightly lower temperature than the other two, indicating a better dispersion between the NPs. In fact, this was the sample that was most easily dispersed in the organic solvent during the preparation of the samples for TEM measurements.

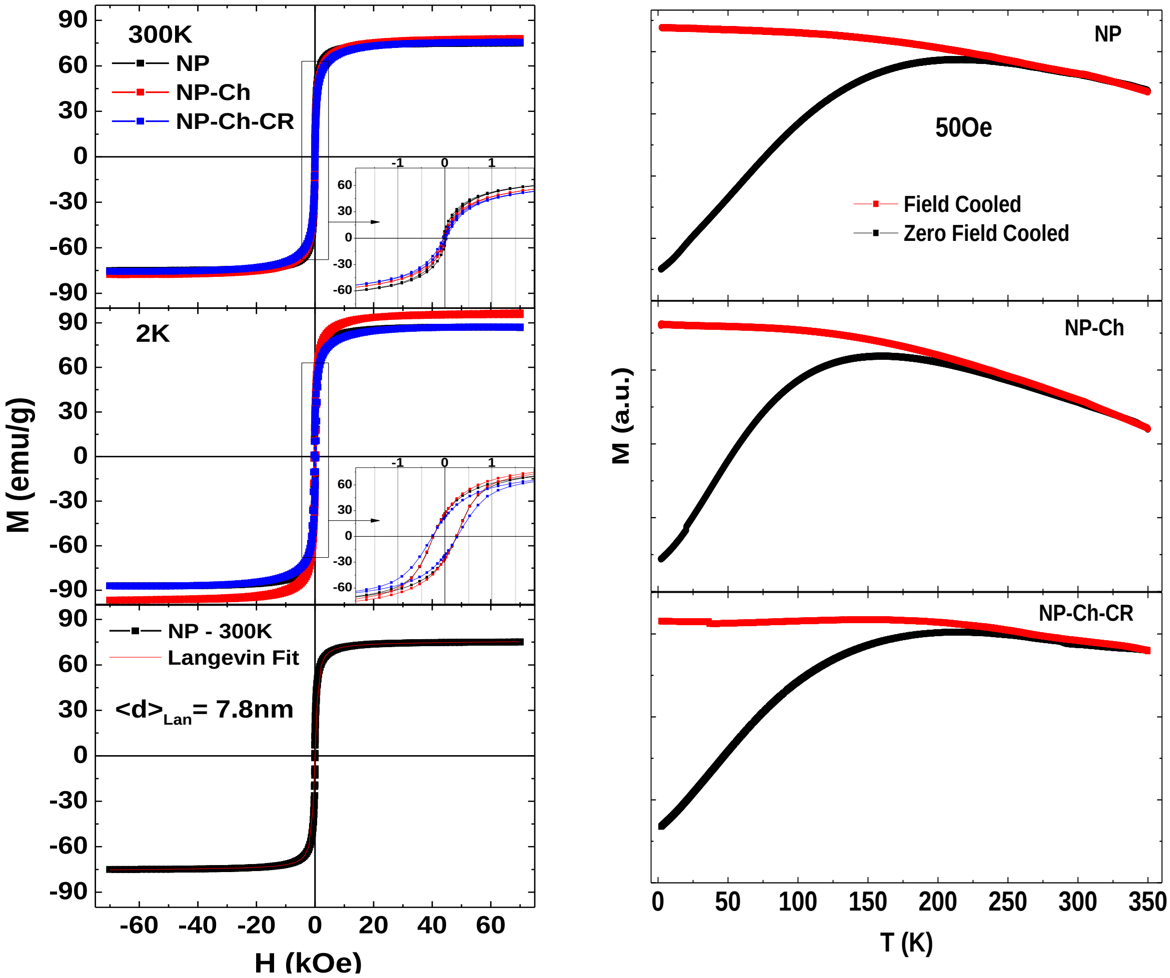

**Fig. 5** Upper left: magnetization (M) as a function of the applied magnetic field (H) measured at 2 and 300 K; the insets show a zoom of the low-field region of the curves; lower left: Langevin fit of the NP sample at 300 K; right: M(T) curves measured at FC (red symbols) and ZFC (black symbols) protocols with H = 50 Oe.

### 3.6 Hydrodynamic size

Dynamic Light Scattering (DLS) measurements were carried out to investigate the hydrodynamic size of bare and coated magnetic nanoparticles under neutral and acidic conditions. It should be taken into account that in this case, the calculated diameters indicate the actual size of the dynamically hydrated and solvated particle/agglomerates, which is usually much larger than the diameter obtained from transmission electron microscope analysis.[76] The analysis of DLS curves (Fig. 6) shows nanoparticle systems forming agglomerates with a broad size distribution for all samples. The mean size of the agglomerates of uncoated nanoparticles was found to be 345 ± 40 nm at pH 7 and 397 ± 45 nm at pH 3. On the other hand, for coated nanoparticles, the mean diameter was 226 ± 13 nm for neutral conditions and 283 ± 19 nm for acidic ones. Evidently, the coating layer of chitosan prevents, to some extent, the formation of larger aggregates of magnetic nanoparticles, leading to a better dispersion of NP-Ch particles in water as compared to naked NP, with even narrower size distribution. The coated nanoparticles show lower particle size as compared to uncoated ones due to the decrease in the agglomerate size by decreasing the dipole–dipole interaction of magnetic iron oxides. The size was reduced by the repulsive forces acting on the particles due to the formation of electrostatic and steric interactions by the presence of chitosan as the coating material. This observation, which was confirmed in other related scientific works,[77-79] is also indirect proof of the presence of chitosan as a shell of the magnetic core. Moreover, similar values were reported in related papers,[76,80-83] even when the synthesis of $Fe_3O_4$ nanoparticles by coprecipitation method has been reported to generate particles with a broad particle size distribution since the molar ratio and salt (chlorides, sulfates, nitrates) of the ferric and ferrous ions, the reaction conditions (temperature, pH, and time), and other parameters such as stirring rate, determine the size and shape of nanoparticles.[80] On the other hand, it is clear that the size of the aggregates obtained by DLS is much larger than those determined by TEM for the corresponding

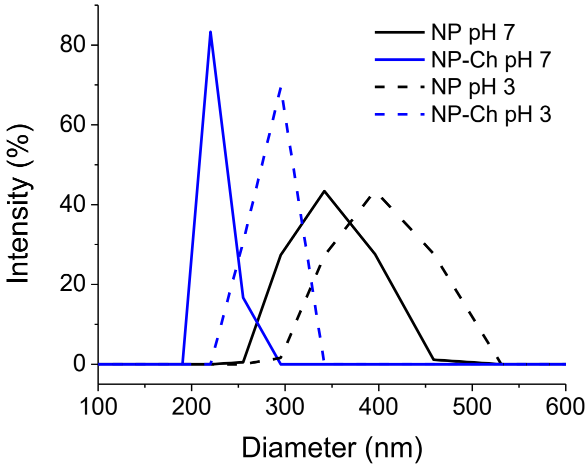

**Fig. 6** DLS results for NP and NP-Ch.

nanoparticles, which was attributed to the tendency of both NP and NP-Ch to form aggregates over time due to their high surface/volume ratio, in good agreement with what has been described in the literature for nanometric particles.[76,81,84]

### 3.7 Colloidal stability

The relative variation of absorbance (*RVA*) was calculated from Equation 3:[41]

$$RVA = \frac{Abs_0 - Abs_t}{Abs_0} \tag{3}$$

where $Abs_0$ and $Abs_t$ are absorbances corresponding to nanoparticles suspensions at 0 and 24 h, respectively. The values obtained for NP and NP-Ch are shown in Table 1.

The colloidal stability of $Fe_3O_4$ nanoparticle suspensions depends on the combined effect of attractive and repulsive forces. Van der Waals forces and magnetic dipole-dipole interactions, generated from residual magnetic moments, are attractive interactions and tend to agglomerate the particles. On the other hand, the repulsive contribution is given by electrostatic interaction and steric hindrance, which plays an important role in stabilizing suspensions.[78] Accordingly, with DLS results, all the samples formed large agglomerates revealing that the suspensions may not be completely stable.

**Table 1.** Relative variation of absorbance of NP and NP-Ch suspensions at different pH within 24 h.

| | pH 7 | pH 3 |
|---|---|---|
| NP | 0.4004 | 0.8999 |
| NP-Ch | 0.7389 | 0.4595 |

Comparatively, NP suspensions are more stable at neutral pH than at acidic ones. The isoelectric point of magnetite nanoparticles is around 6.85[41,85,86] and thus, at pH below it, the particle surfaces are positively charged because of the formation of $FeOH_2^+$ groups, while above it they are negatively charged due to the formation of $FeO^-$ groups.[41,85,86] At neutral essay conditions, which are near the isoelectric point, the surfaces of the particles do not possess enough charge to repel from each other thus stabilizing the suspension. Nevertheless, there are other effects apart from surface charges such as gravitational forces, high surface/volume ratio of the nanoparticles as discussed above, and elastic work in the case of mechanically soft particles, which also affect suspension stability.[87] At acid pH, sulfate ions interact with the magnetite surface affecting its zeta potential ($\xi$). Mansour *et al*.[88] found that the $\xi$ of magnetite particles do not change above the isoelectric point at high concentrations of sulfate, but lower it below this point, practically leading to neutral surfaces. Since the acid suspension conditions were obtained by the addition of sulfuric acid, it is expected that the surface charge of NP is low and thus the particles tend to agglomerate and precipitate leading to an unstable suspension. These results agree with those previously observed in DLS studies.

Chitosan coating should contribute to the stabilization of the suspension because it provides the NP with a steric hindrance. The isoelectric point of chitosan is around 6.3,[78] therefore at neutral conditions, the NP-Ch surface charge is overmuch low to maintain the suspension stable despite the chitosan coating, and nanoparticles and their agglomerates precipitate after 24 h. At low pH, the protonation of free amino groups contained in the chitosan backbone occurs, making the surface charge more positive.[78] A more positive surface charge added to the steric hindrance makes the suspension somewhat more stable than at neutral conditions. However, it is worth mentioning that the orbital agitation supplied for the adsorption assays reported in the next section was sufficient to keep both types of particles in suspension and limit the formation of aggregates during the entire duration of the tests.

### 3.8 Adsorption tests

#### 3.8.1 Kinetic adsorption studies

The adsorption kinetic results using NP and NP-Ch as adsorbents and different initial concentrations of CR solutions (10 mg $L^{-1}$ and 100 mg $L^{-1}$, respectively) are shown in Figs. 7a and 7b. The pH during the experiments was in the range of 6.5-7. It is clearly observed that the polymeric coating is essential to achieve a significant colorant removal, in contrast to uncoated particles, which present an erratic behavior attributable to surface oxidation[23] and lower adsorption capacity in the pH range analyzed in this experiment. Since in the present cases the tests were carried out close to the isoelectric point of magnetite (~6.85), small variations in the pH of the CR solutions can favor the obtaining of iron oxides particles with different and opposite charges and consequently,

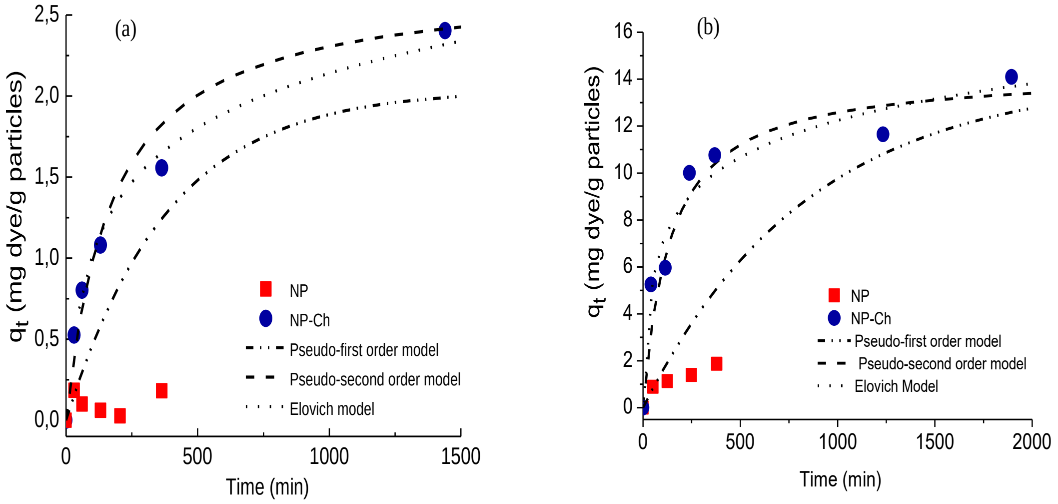

**Fig. 7** Adsorption kinetics for different CR initial concentrations; (a) 10 mg L$^{-1}$ (b) and 100 mg L$^{-1}$.

these erratic adsorption behavior can be expected. On the other hand, the biopolymer and the magnetic nanoparticles develop strong and synergic interactions[48] that are denoted in the higher adsorption capacity of NP-Ch than the control sample (NP), which increases as the concentration of the dye solution increases.

The kinetic results obtained with NP-Ch were theoretically modeled using the pseudo-first-order model, pseudo-second-order model, and Elovich model. The linear equation of the pseudo-first-order model can be expressed with Equation 4:

$$\ln(q_e - q_t) = \ln(q_e) - k_1 t \tag{4}$$

where $k_1$ (min$^{-1}$) stands for the rate constant of pseudo-first-order kinetics. $q_t$ and $q_e$ (mg g$^{-1}$) represent the adsorption capacity of adsorbents at time $t$ and equilibrium time (min), respectively. The linear form of the pseudo-second-order equation is presented in Equation 5:

$$\frac{t}{q_t} = \frac{1}{k_2 {q_e}^2} + \frac{1}{q_e} t \tag{5}$$

where $k_2$ (g (mg min)$^{-1}$) is the kinetic equilibrium constant. Moreover, the Elovich model can be written as follows in Equation 6:

$$q_t = \frac{1}{\beta}\ln(\alpha\beta) + \frac{1}{\beta}\ln t \tag{6}$$

where $\alpha$ (mg (g min)$^{-1}$) and $\beta$ (g mg$^{-1}$) corresponds to the initial adsorption rate and the desorption constant of the Elovich model, respectively.[89, 90]

Figures 7a and 7b also exhibit fitted plots of the three kinetics models on the experimental data of Congo red adsorption at different concentrations. The obtained parameters are summarized in Table 2 for both CR solution concentrations.

**Table 2.** Calculated parameters of different models for modeling kinetic adsorption results.

| Initial concentration | 10 mg L$^{-1}$ | 100 mg L$^{-1}$ |
|---|---|---|
| Pseudo-first order model | | |
| $k_1$ (min$^{-1}$) | 0.0026 | 0.0018 |
| $q_e$ (mg L$^{-1}$) | 2.0598 | 8.4267 |
| $R^2$ | 0.9000 | 0.5733 |
| Pseudo-second order model | | |
| $k_2$ (g (mg min)$^{-1}$) | 0.0021 | 0.0005 |
| $q_e$ (mg L$^{-1}$) | 2.7079 | 14.3328 |
| $R^2$ | 0.9881 | 0.9829 |
| Elovich model | | |
| α (mg (g min)$^{-1}$) | 0.0402 | 0.5019 |
| β (g mg$^{-1}$) | 2.0631 | 0.4412 |
| $R^2$ | 0.9835 | 0.8947 |

The experimental values of adsorption capacity as a function of the time present the best fit with the pseudo-second-order model ($R^2$ = 0.9881/0.9829, Table 2), independently of dye concentration. This kinetic model is based on the assumption that the rate-limiting step is the chemical sorption or chemisorption[17,68] and predicts the behavior over the whole range of adsorption. In this condition, the adsorption rate is dependent on adsorption capacity. That is to say, the adsorption was mainly controlled by chemical adsorption that depends on the electron sharing or electron exchange between adsorbent and adsorbate.[91] Moreover, one major advantage of this model over that of Elovich is that the equilibrium adsorption capacity can be calculated from the model; therefore, there is theoretically no need to evaluate adsorption equilibrium capacity from experiments.[92] $k_2 {q_e}^2$, a parameter that represents initial adsorption velocity,[92] is greater for 100 mg L$^{-1}$ initial concentration, since in this condition there is a bigger difference between CR solution concentration and CR adsorbed on the particles, expressed on the same basis. Moreover, during this first adsorption stage, the CR mainly adsorbs on the particle surface and once most of these adsorption sites are occupied, the second stage begins, during which the dye molecules start to enter the pores and are adsorbed in the interior place. Based on these results, it can be concluded that the adsorption of the dye mainly takes place via the surface exchange reactions until the surface active sites are completely occupied; thereafter dye molecules may diffuse into the metal-organic framework structure for further interactions and/or reactions such as ion-exchange or complexation, as was reported in related papers.[17,46] On the other hand, the Elovich model describes the chemisorption processes by assuming that the reactive sites on the adsorbent with complex surfaces have heterogeneous energy.[93] $R^2$ values of 0.9835 and 0.8947 for 10 mg $L^{-1}$ and 100 mg $L^{-1}$, respectively, showed that the Elovich model was also applicable to our data, although with a poorer fit. The values of $\alpha$ increase with concentration for the same reason that $k_2q_e^2$ from the pseudo-second-order model changes, while $\beta$ decreases with initial concentration due to the relative reduction of available solid surface for CR dye adsorption.[94] In the same line, the pseudo-first-order model provides a rather poor fit for the adsorption data at 10 mg $L^{-1}$ but fails in modeling the results of concentrated solutions, which was attributed to that this model follows Lagergren's kinetic and describes the adsorption as a physisorption process.[86]

### 3.8.2 Equilibrium adsorption studies

The adsorption capacities of core-shell NP-Ch obtained at equilibrium conditions (i.e. 24 h) in contact with different initial concentrations of CR were measured. The results of equilibrium adsorption capacity, $qe$ vs. CR initial concentration, $C_0$, at two different pHs (pH~7 and pH~3), are shown in Fig. 8. The trend shows that the adsorption capacity at equilibrium is a linear function of the CR initial concentration when solutions of neutral pH are treated, but a different trend is noticed in acidic conditions. The solution pH can affect the surface charge of the adsorbent, the degree of ionization of the organic pollutants, the dissociation of the functional groups on the active sites of the adsorbent as well as the dye structure.[17] In the present case, it is expected that the surface charge of chitosan-coated NP was positive in acidic pH and decreased gradually with an increase in pH, passing through zero potential at about pH 6.4.[39] In the acidic pH range, the surface charge of the adsorbent increases mainly due to increased protonation of the amine group ($-NH_3^+$) of chitosan, and since Congo red is an acidic dye that contains negatively charged sulfonated group ($-SO_3^-$ $Na^+$), higher adsorption of the dye at low pH due the increase in electrostatic attraction between the negatively charged dye molecule and the positively charged amine group of chitosan is expected. Even so, from both kinetics and equilibrium studies, it is clear that the chemisorption mechanism might be operative still at neutral pH since significant adsorption of the anionic dye onto chitosan-coated magnetic iron oxide still occurred at alkaline pH values, as was also reported in related papers.[39,95] In this regard, a proposed adsorption mechanism of CR on NP-Ch is presented in Scheme 2. According to the results obtained in this work as well as previous results on similar systems,[39] it is inferred that the adsorption driving forces may include two parts: electrostatic attraction as well as hydrogen bonding. The electrostatic attraction is due to the protonated amino groups of chitosan chains and the sulfonate groups of the dye and it is the main mechanism for adsorption at acidic pH, as is also indicated in the related bibliography.[96,97]

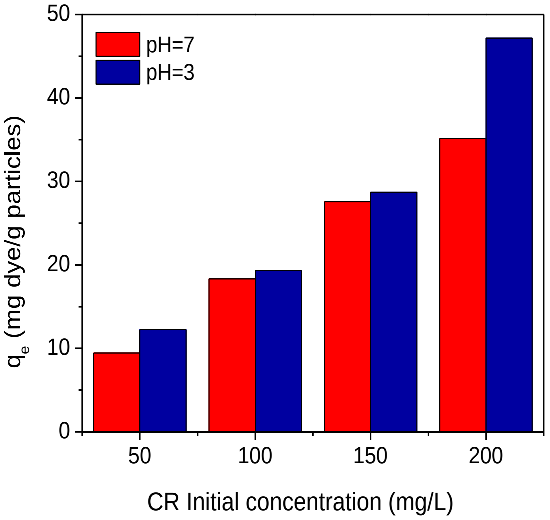

**Fig. 8** Equilibrium adsorption as a function of CR initial concentration and different pH.

Experimental results were modeled theoretically for both pH conditions using Langmuir, Freundlich, and Dubinin-Radushkevich (D-R) isotherms. The nonlinear form of the Langmuir equation can be represented as follows in Equation 7:

$$q_e = \frac{q_{max}K_LC_e}{1+K_LC_e} \quad (7)$$

where $C_e$ is the equilibrium concentration of adsorbate (mg $L^{-1}$); $q_e$ is the equilibrium adsorption capacity (mg $g^{-1}$), $q_{max}$ is the maximum adsorption capacity of the adsorbate (mg $g^{-1}$), and $K_L$ represents the affinity constant (L $mg^{-1}$). This model is based on the assumption that the adsorption process takes place at specific homogeneous sites within the adsorbent surface and that once a metal ion occupies a site, no further adsorption can take place at that site, that is, it assumes that the adsorption process is monolayer in nature. For predicting the favorability of an adsorption system, the Langmuir

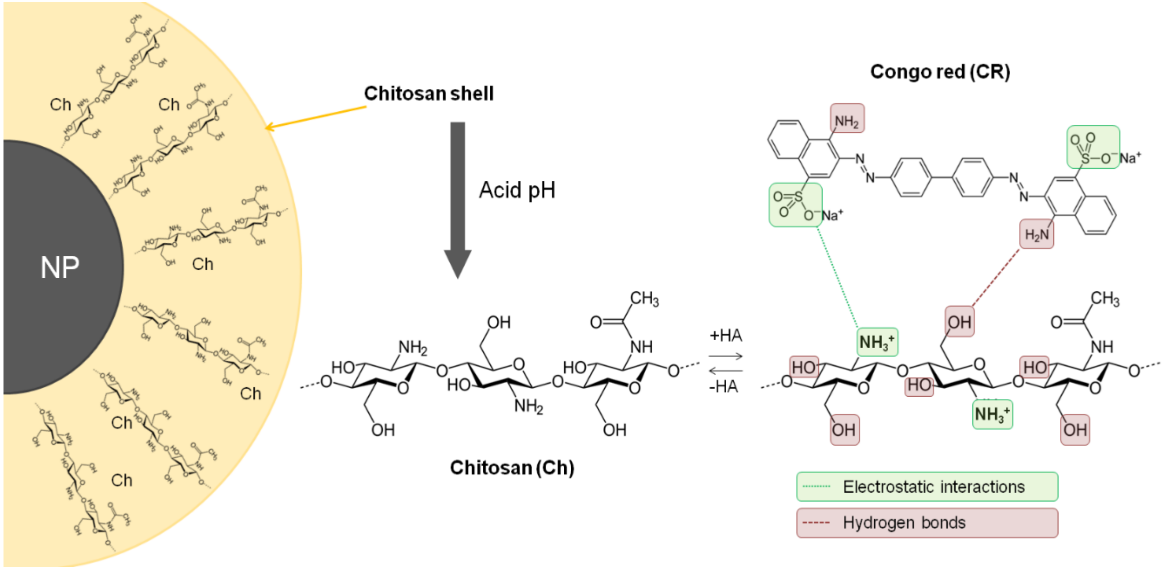

**Scheme 2** Proposed adsorption mechanism of Congo red onto NP-Ch.

equation can also be expressed in terms of a dimensionless separation factor $R_L$ defined as Equation 8:

$$R_L = \frac{1}{1+C_0 K_L} \tag{8}$$

where $C_0$ is the maximum initial concentration of adsorbate (mg $L^{-1}$) and $R_L$ indicates the favorability of the adsorption system, resulting in irreversible, favorable, linear, or unfavorable adsorption isotherms for $R_L=0$, $0 < R_L < 1$, $R_L=1$, *and* $R_L > 1$, respectively.

Equation 9 represents the Freundlich isotherm as follows:

$$q_e = K_F C_e^{1/n} \tag{9}$$

Where $K_F$ ((mg $g^{-1}$)(L $mg^{-1}$)$^{1/n}$) and $n$ (dimensionless) are the Freundlich constants related to the maximum adsorption capacity[98] and intensity (or heterogeneity factor), respectively.[17,46] The Freundlich isotherm is an empirical equation that assumes that the surface of the adsorbent is heterogeneous and the adsorption capacity depends upon the concentration of the adsorbate, thus involving the interaction between adsorbed molecules,[17,46,99] which is suitable for modeling adsorption on highly hybrid surfaces lacking saturated adsorption platforms.[100]

Dubinin-Radushkevich isotherm equation can be written as follows in Equation 10:

$$\ln(q_e) = \ln(q_m) - \beta\, \varepsilon^2 \tag{10}$$

where $q_e$ (mg $g^{-1}$) is the amount of the dye adsorbed per unit weight of the adsorbent, $q_m$ is the D–R adsorption capacity (mg $g^{-1}$), and $\beta$ is a constant related to adsorption energy (mol$^2$ $J^{-2}$). $\varepsilon$ (J $mol^{-1}$) is the Polanyi potential calculated from Equation 11:

$$\varepsilon = R\,T \ln\left(1 + \frac{1}{C_e}\right) \tag{11}$$

where $R$ is the gas constant (8.314 J (mol K)$^{-1}$) and $T$ the absolute temperature (K), which is 298 K in this case.

The experimental results were modeled theoretically for both pH conditions using these three isotherms and the fitting curves are displayed in Fig. 9. Furthermore, the calculated parameters from Langmuir isotherm ($q_{max}$ and $K_L$), Freundlich isotherm ($n$ and $K_F$) and Dubinin-Radushkevich isotherm ($q_m$ and $\beta$) along with their corresponding regression coefficients ($R^2$) for the Congo red adsorption onto NP-Ch are shown in Table 3. The parameters obtained with the Langmuir isotherm for acidic conditions were negative, indicating the lacking of physical sense or, in the best case, an unfavorable adsorption isotherm ($R_L > 1$).

**Table 3.** Parameters are calculated from the different models used in the modeling of equilibrium adsorption results.

| Initial pH | 7 | 3 |
|---|---|---|
| Langmuir model | | |
| $K_L$ (L $mg^{-1}$) | 0.9672 | - |
| $q_{max}$ (mg $g^{-1}$) | 36.8186 | - |
| $R^2$ | 0.9998 | - |
| Freundlich model | | |
| $K_F$ (mg $g^{-1}$)(L $mg^{-1}$)$^{1/n}$) | 15.8646 | 0.6947 |
| n | 3.2612 | 0.4242 |
| $R^2$ | 0.7977 | 0.9802 |
| Dubinin-Radushkevich model | | |
| $q_m$ (mg $g^{-1}$) | 29.3080 | 69.1460 |
| $\beta$ (mol$^2$ $J^{-2}$) | 1.04 $10^{-7}$ | 3.51 $10^{-6}$ |
| $R^2$ | 0.8629 | 0.7099 |

At neutral conditions, the best fit ($R^2$=0.9998) was achieved with Langmuir isotherm. Since in this case both $K_L$ and any $C_0$ are positive numbers, the value of $R_L$ is between 0 and 1, indicating a favorable adsorption process.[101] An

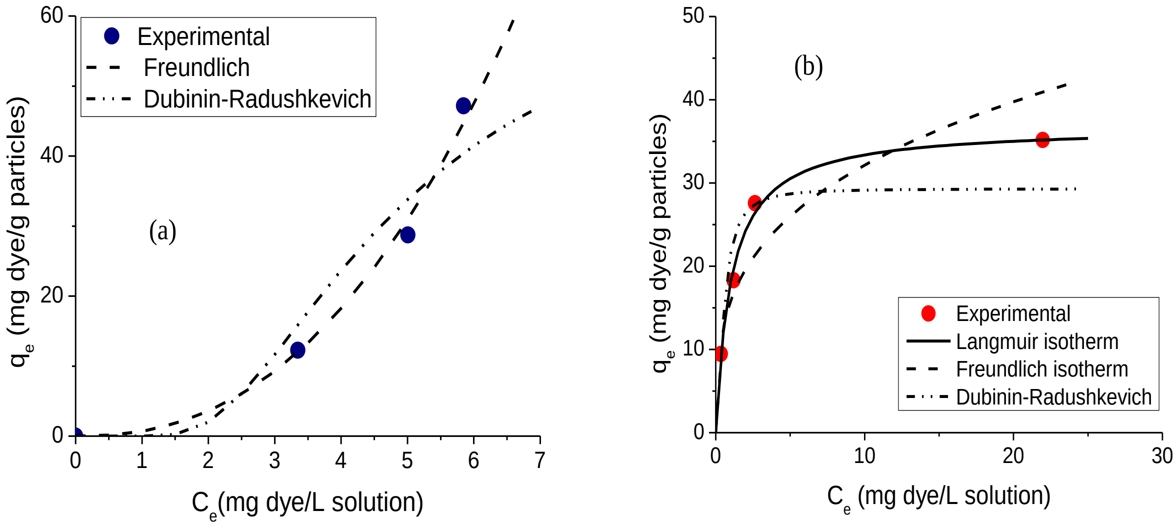

**Fig. 9** Fitting of experimental points with different isotherms: (a) pH≈7, (b) pH≈3.

advantage of the Langmuir model is that it easily allows comparing the maximum adsorption capacity among different adsorbents. As previously indicated, our easy synthesis procedure endowed NP-Ch particles with $q_{max}$ = 36.819 mg g$^{-1}$, while similar particles prepared by Zhu *et al.*[95] through a methodology a bit more complicated that also involves longer synthesis times than ours obtained a Langmuir maximum adsorption capacity of 42.62 ± 1.14 mg g$^{-1}$ at 295 K, which increases to 56.66 ± 2.79 mg g$^{-1}$ at 315 K. On the other hand, Khan *et al.*,[98] obtained a $q_{max}$ = 93.4 mg g$^{-1}$ for their chitosan-capped Fe$^0$-based Fe-Pd-Ir (Chi-Fe-Pd-Ir) tri-metallic nanoparticles, fabricated using metal displacement method in presence of sodium borohydride, which is a more complex synthesis procedure.

The pH dependence of the adsorption process, which reveals also a change in the mechanism of the adsorption, can be confirmed by modeling the experimental data obtained at acidic conditions. In this case, the Freundlich isotherm provides a fairly acceptable fit ($R^2$=0.9802) of the experimental data (Fig. 9b). It should be taken into account that $n$ values higher than 1 indicate favorable adsorption isotherm,[39,98] which is clearly not the present case although the $qe$ values obtained experimentally for each $C_0$ are higher than those measured at neutral pH.

The mean free energy of adsorption ($E$) is the free energy change when one mole of ion is transferred to the surface of the adsorbent from infinity in the solution[102,103] and can be calculated from $\beta$ values of the D-R model according to Equation 12:

$$E = \frac{1}{\sqrt{2\,\beta}} \tag{12}$$

When $E < 8$ kJ mol$^{-1}$, the adsorption process can be explained by physical adsorption, for $E$ between 8 and 16 kJ mol$^{-1}$ the adsorption corresponds to ion exchange processes, and if $E$ above 16 kJ mol$^{-1}$, it is attributed to stronger chemical adsorption than ion exchange.[104] The values of $E$ found in this work were 2.194 kJ mol$^{-1}$ for neutral conditions and 0.3775 kJ mol$^{-1}$ for acid conditions suggesting the high contribution of physic-sorption for the adsorption of Congo red. However, as can be noticed from Table 3, the $R^2$ values of the D–R isotherm model are lower than the Langmuir and Freundlich values for neutral and acid conditions, respectively, so this outcome must be taken with care.

### 3.9 Thermodynamics of adsorption

A basic thermodynamic analysis was also conducted in this case: the standard free energy change ($\Delta G_0$) was calculated as $\Delta G_0 = -R\,T \ln K$[27,28,39,105] where $R$ is the gas constant (8.314 J mol$^{-1}$ K$^{-1}$), $T$ is the absolute temperature (298 K in this case) and $K$ is adsorption equilibrium constant. For conditions where the adsorbent follows the Langmuir isotherm (neutral pH), the equilibrium constant ($K$) can be related to the Langmuir constant $K_L$ (with units of L mol$^{-1}$) as $K = 55.5\,K_L$, where the value 55.5 corresponds to the molar concentration of the solvent (in this case water) with units of mol L$^{-1}$.[106] The $\Delta G_0$ value obtained in this case is -9.87 kJ mol$^{-1}$.

A similar analysis was also conducted, by using the standard Gibbs energy change ($\Delta G^0$) that can be calculated using the van't Hoff equation (Equation 13):

$$\Delta G^0 = -R\,T \ln K^0_{Eq} \tag{13}$$

where $K^0_{Eq}$ is the dimensionless, standard thermodynamic equilibrium constant. According to Tran,[107] $K^0_{Eq}$ should be obtained from Equation 14:

$$K^0_{Eq} = \frac{K_L}{\gamma_{Adsorbate}} C^0 \tag{14}$$

in which $K_L$ (L mg$^{-1}$) is the Langmuir adsorption equilibrium constant, $\gamma_{Adsorbate}$ (dimensionless) is the activity coefficient of adsorbate and $C^0$ is the standard concentration of the adsorbate. $\gamma_{Adsorbate}$ can be considered = 1.0 under dilute conditions, when ionic strength is lower than 0.001 mol $L^{-1}$,[108] and, according to IUPAC, the recommended value for standard thermodynamic quantities is $C^0 = 1$ mol $dm^{-3}$.[107] Moreover, in order to get the dimensionless $K^0_{Eq}$ value, $K_L$ in Eq. 14 should be affected by CR molecular weight (696.7 g $mol^{-1}$) and a 1000 mg $g^{-1}$ factor.[109]

For neutral conditions $K^0_{Eq}$ results 6.74 $10^5$ and, therefore, $\Delta G^0$ is -33.25 kJ $mol^{-1}$. As in the previous case, the negative value of the standard Gibbs energy confirms the feasibility of the adsorption of Congo red dye under these conditions and that the analysis cannot be carried out for adsorption conditions in an acidic medium. Indeed, although $K_L$ in Eq. 14 can be replaced with other constants, they must have units of L $mg^{-1}$, and Freundlich or D-R constants do not satisfy this condition. Furthermore, thermodynamic parameters calculated based on $K_F$ do not bring physical meanings.[107]

On the other hand, when the adsorption process is carried out by the interaction of a solution with a solid adsorbent, the change in the chemical potential of the system can be calculated if the initial and equilibrium concentrations ($C_0$ and $C_e$, respectively) are known, as follows in Equation 15:

$$\Delta\mu = RT \ln\left(\frac{C_e}{C_0}\right) \tag{15}$$

and since $C_e/C_0$ relationship can be taken as the adsorption equilibrium constant of the transient adsorption process, the chemical potential calculated in this way also could be ascribed to the change in the molar free energy of the adsorption process.[110] Therefore, the obtained standard free energy changes for both neutral and acid conditions using Eq. 15 were calculated and are reported in Table 4.

**Table 4.** Standard free energy change ($\Delta G_0$) for the adsorption of Congo red at 298 K and different dye concentrations and pH conditions.

| pH condition | $C_0$ (mg $L^{-1}$) | $C_e$ (mg $L^{-1}$) | $\Delta G_0$ (kJ $mol^{-1}$) |
|---|---|---|---|
| Neutral | 50 | 0.362 | -12.20 |
| | 100 | 1.155 | -11.05 |
| | 150 | 2.581 | -10.06 |
| | 200 | 21.970 | -5.47 |
| Acidic | 50 | ~0 | - |
| | 100 | 3.367 | -8.40 |
| | 150 | 5.013 | -8.42 |
| | 200 | 5.838 | -8.75 |

From Table 4 it is clear that all calculated values are negative since $C_e$ is always lower than $\mathbf{C_0}$, which confirms the feasibility and spontaneous nature of the adsorption of Congo red dye under both, neutral and acidic conditions. Moreover, the obtained $\Delta G_0$ values are comparable with the values reported for similar systems and conditions.[28,105] Additionally, it can be noticed that for neutral conditions the absolute value of $\Delta G_0$ decreases as the initial concentration of the CR solution increases while in acidic conditions it does just the opposite, confirming that the adsorption mechanism is pH dependent.

To summarize this section, it is interesting to notice that, although the calculated $\Delta G^0$ values differ according to the methodology selected for the calculation of the equilibrium constant, the obtained values are always negative and, in general, one order of magnitude less than those of other adsorbent materials.[111]

### 3.10 Stability and reusability/desorption

The stability and reusability of an adsorbent are important indexes for practical applications. NP-Ch stability was evaluated by washing the NP-Ch in ethanol (96%) in the last step of the purification process using ultra-centrifugation to separate the particles from the solvent. Other samples were tested in two aqueous sulfuric acid solutions (pH = 4.1 and 2.7) by orbital shaking at 100 rpm for 24 hours. Those samples were washed with distilled water until neutral pH, separating the particles by magnetic decantation after each washing step. Finally, the washed particles were dried until reaching constant mass and tested in a TGA analyzer. Surprisingly, no mass loss was observed in any of the samples with respect to the original particles, which indicates that chitosan coating is firmly attached to the magnetic core but also that Fe's leaching was effectively prevented even at extremely acidic conditions. Another important factor related to the use of adsorption processes in industrial applications is the possibility to reuse the adsorbent materials. Thus, a procedure consisting of subjecting the CR-saturated NP-Ch to a 1-day immersion in highly alkaline NaOH solutions, that could promote the desorption of anionic dyes[112] was tested as an attempt to regenerate the adsorbent. As expected, once the particles were placed in the alkaline solution (initially colorless), they started to gain a reddish color, thus, the dye concentration at the end of the immersion period was measured by UV spectroscopy.

The results obtained are shown in Fig. 10, in which exactly the same particles used to measure equilibrium adsorption at pH ~ 3 were separated from the adsorbent solution and subsequently transferred to the alkaline solution.

The percentage of colorant desorbed from NP-Ch from the pH 3 experiment is around 50% in all the studied cases (Fig. 10b). Although this result is preliminary, indicates the possibility to reuse the adsorbent material and encourages us to continue looking for alternative procedures to achieve more

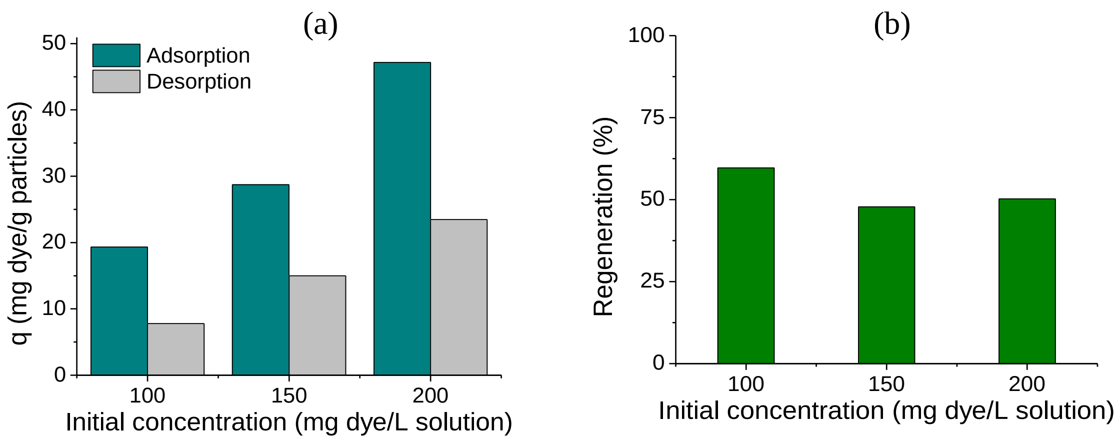

**Fig. 10** a) CR adsorbed onto NP-Ch before and after the desorption test. b) Regeneration percentage as a function of the initial concentration of CR in NP-Ch particles.

complete desorption.

## 4. Conclusions

This paper reported the results of a systematic study that started from the obtaining and physical, chemical, and magnetic characterization of adsorbent nanoparticles and concluded with the analysis of their performance as Nano adsorbents of a toxic synthetic dye widely used in the textile industry. Accordingly, iron oxide nanoparticles coated with chitosan were prepared and tested as potential adsorbent material for Congo red. The particles presented a good magnetic response that facilitates their separation from contaminant or dye solutions. Their nanometer size was proved through XRD and TEM, which demonstrates also that the particle and crystallite sizes are similar. The presence of the polymer coating, on the other hand, was confirmed through FTIR, TGA, and XPS analysis. Furthermore, dynamic light scattering revealed that NP and NP-Ch aqueous suspensions formed agglomerates with a broad size distribution both in neutral and acidic conditions, although the chitosan coating reduced, to some extent, the agglomerate mean size. Since the NP-Ch suspensions are not completely stable, the agitation should be maintained during the adsorption test in order to achieve the reported adsorption capacity.

Chitosan coating was responsible for the good adsorption capacity achieved under the different conditions studied via both the chemisorption mechanism and electrostatic attraction due to the presence of amino groups in its backbone. As a general trend, it was found that the equilibrium adsorption capacity increases with the increased initial dye concentration and decreases with the increase of pH, which is related to the driving force of the concentration gradient and to the reduction of electrostatic interactions (i.e. decrease of the amount of positively charged amine group of chitosan), respectively.

The results from the different adsorption experiments were best theoretically adjusted with the pseudo-second model and Langmuir or Freundlich isotherms, depending on the pH conditions. The maximum adsorption capacity obtained by modeling the experimental data according to Langmuir isotherm was compared to those obtained using similar adsorbents and found to be somewhat lower, although it was also highlighted that the synthesis procedure used in this work is much simpler and less time-consuming. The $\Delta G_0$ values for all tested adsorption processes are negative, which confirms the feasibility and spontaneous nature of the adsorption of Congo red dye under the conditions selected in this work.

## Acknowledgments

The authors gratefully acknowledge the financial support provided by the Science and Technology National Promotion Agency (ANPCyT, PICT-2017-1318, and PICT 2019-2677, PICT 2021-0153), the National University of Mar del Plata (15/G625 - ING629/21 Project), the Scientific Research Commission of the Province of Buenos Aires (CIC) for the training scholarship granted to Eng. Melina Kloster and the LNNano (Proposal 20230478).

## Conflict of Interest

There is no conflict of interest.

## Supporting Information

Not applicable.

## References

[1] K. M. Hassan, The role of magnetite/graphene oxide nano-composite as a high-efficiency adsorbent for removal of phenazopyridine residues from water samples, an experimental/theoretical investigation, *Journal of Molecular Liquids*, 2020, **298**, 112040, doi: 10.1016/j.molliq.2019.112040.

[2] R, Jothirani, Ultrasonic modified corn pith for the sequestration of dye from aqueous solution, *Journal of Industrial and Engineering Chemistry*, 2016, **39**, 162-175, doi: 10.1016/j.jiec.2016.05.024.

[3] V, Tharaneedhar, Prediction and interpretation of adsorption parameters for the sequestration of methylene blue dye from aqueous solution using microwave assisted corncob activated carbon, *Sustainable Materials and Technologies*, 2017, **11**, 1-11, doi: 10.1016/j.susmat.2016.11.001.

[4] O. Jinbo, Biomass-derived activated carbons for the removal of pharmaceutical mircopollutants from wastewater: a review, *Separation and Purification Technology*, 2020, **253**, 117536, doi: 10.1016/j.seppur.2020.117536.

[5] Jianlong, Wang, Removal of pharmaceuticals and personal care products (PPCPs) from wastewater: a review, *Journal of Environmental Management*, 2016, **182**, 620-640, doi: 10.1016/j.jenvman.2016.07.049.

[6] M. C. Ncibi, B. Mahjoub, O. Mahjoub, M. Sillanpää, Remediation of emerging pollutants in contaminated wastewater and aquatic environments: biomass-based technologies, CLEAN - Soil, Air, Water, 2017, **45**, 1700101, doi: 10.1002/clen.201700101.

[7] H. Singh, S. Choden, Comparison of adsorption behaviour and kinetic modeling of bio-waste materials using basic dye as adsorbate, *Indian Journal of Chemical Technology (IJCT)*, 2016, **21**, 359-367.

[8] Y. Wang, H. Wang, X. Wang, Y. Xiao, Y. Zhou, X. Su, J. Cai, F. Sun, Resuscitation, isolation and immobilization of bacterial species for efficient textile wastewater treatment: a critical review and update, *Science of the Total Environment*, 2020, **730**, 139034, doi: 10.1016/j.scitotenv.2020.139034.

[9] V. Kumar, B. S. Giri, N. Raza, K. Roy, K-H Kim, B N Rai, R. S. Singh, Recent advancements in bioremediation of dye: current status and challenges, *Bioresource Technology*, 2018, **253**, 355-367, doi: 10.1016/j.biortech.2018.01.029.

[10] S. Raj, H. Singh, J. Bhattacharya, Treatment of textile industry wastewater based on coagulation-flocculation aided sedimentation followed by adsorption: process studies in an industrial ecology concept, *Science of the Total Environment*, 2023, **857**, 159464, doi: 10.1016/j.scitotenv.2022.159464.

[11] V. Chittal, M. Gracias, A. Anu, P. Saha, K. V. Bhaskara Rao, Biodecolorization and biodegradation of azo dye reactive orange-16 by marine nocardiopsis sp, *Iranian Journal of Biotechnology*, 2019, **17**, 18-26, doi: 10.29252/ijb.1551.

[12] D. Bhatia, N. R. Sharma, R. Kanwar, J. Singh, Physicochemical assessment of industrial textile effluents of Punjab (India), *Applied Water Science*, 2018, **8**, 1-12, doi: 10.1007/s13201-018-0728-4.

[13] M.R. Al-Mamun, S. Kader, M.S. Islam, M.Z.H. Khan, Photocatalytic activity improvement and application of UV-$TiO_2$ photocatalysis in textile wastewater treatment: a review, *Journal of Environmental Chemical Engineering*, 2019, **7**, 103248, doi: 10.1016/j.jece.2019.103248.

[14] K. Hunger, Dyes, general survey. Industrial Dyes: Chemistry, Properties, Applications, Wiley Subscription Services, Inc., A Wiley Company, Frankfurt, 2003, 1-10.

[15] M. Kumar, H. S. Dosanjh, H. Singh, Magnetic zinc ferrite-chitosan bio-composite: synthesis, characterization and adsorption behavior studies for cationic dyes in single and binary systems, *Journal of Inorganic and Organometallic Polymers and Materials*, 2018, **28**, 880-898, doi: 10.1007/s10904-017-0752-0.

[16] M. Hui, S. Pu, Y. Hou, R. Zhu, A. Zinchenko, W. Chu, A highly efficient magnetic chitosan “fluid” adsorbent with a high capacity and fast adsorption kinetics for dyeing wastewater purification, *Chemical Engineering Journal*, 2018, **345**, 556-565, doi: 10.1016/j.cej.2018.03.115.

[17] S. Dadfarnia, A. M. Haji Shabani, S. E. Moradi, S. Emami, Methyl red removal from water by iron-based metal-organic frameworks loaded onto iron oxide nanoparticle adsorbent, *Applied Surface Science*, 2015, **330**, 85-93, doi: 10.1016/j.apsusc.2014.12.196.

[18] G. Mohammad, Mahfouz, Uranium extraction using magnetic nano-based particles of diethylenetriamine-functionalized chitosan: equilibrium and kinetic studies, *Chemical Engineering Journal*, 2015, **262**, 198-209, doi: 10.1016/j.cej.2014.09.061.

[19] M. Kumar, H. S. Dosanjh, H. Singh, Biopolymer modified transition metal spinel ferrites for removal of fluoride ions from water, *Environmental Nanotechnology, Monitoring & Management*, 2019, **12**, 100237, doi: 10.1016/j.enmm.2019.100237.

[20] Md N. Sakib, N. Hano b, M. Takafuji, S. Ahmed, Preparation of chitosan/laterite/iron oxide-based biocomposite and its application as a potential adsorbent for the removal of methylene blue from aqueous solution, *Environmental Nanotechnology, Monitoring & Management*, 2022, **17**, 100658, doi: 10.1016/j.enmm.2022.100658.

[21] S. R. Chowdhury, E. K. Yanful, A. R. Pratt, Chemical states in XPS and Raman analysis during removal of Cr(VI) from contaminated water by mixed maghemite-magnetite nanoparticles, *Journal of Hazardous Materials*, 2012, **235-236**, 246-256, doi: 10.1016/j.jhazmat.2012.07.054.

[22] I. Alfaro, L. Molina. P. González, J. Gaete, F. Valenzuela, J. F. Marco, C. Sáez, C. Basualto, Silica-coated magnetite nanoparticles functionalized with betaine and their use as an adsorbent for Mo(VI) and Re(VII) species from acidic aqueous solutions, *Journal of Industrial and Engineering Chemistry*, 2019, **78**, 271-283, doi: 10.1016/j.jiec.2019.06.002.

[23] Q. Kaili, T. Weijun, B. Jie, W. Liang, Z. Jing, D. Zhaoyang, G. XiaoxiApplication of magnetic adsorbents based on iron oxide nanoparticles for oil spill remediation: a review, *Journal of the Taiwan Institute of Chemical Engineers*, 2019, **97**, 227-236, doi: 10.1016/j.jtice.2019.01.029.

[24] A.-H. Lu, E. L. Salabas, F. Schüth, Magnetic nanoparticles: synthesis, protection, functionalization, and application, *Angewandte Chemie International Edition*, 2007, **46**, 1222-1244, doi: 10.1002/anie.200602866.

[25] T. M, Aljarrah, in situ synthesis of quaternary ammonium on silica-coated magnetic nanoparticles and it’s application for the removal of uranium (VI) from aqueous media, *Journal of*

*Environmental Chemical Engineering*, 2018, **6**, 5662-5669, doi: 10.1016/j.jece.2018.08.070.

[26] X. Yang, Y. Li, H. Gao, C. Wang, X. Zhang, H. Zhou, One-step fabrication of chitosan-Fe(OH)$_3$ beads for efficient adsorption of anionic dyes, *International Journal of Biological Macromolecules*, 2018, **117**, 30-41, doi: 10.1016/j.ijbiomac.2018.05.137.

[27] C. Jeyaseelan, N. Chaudhary, R. Jugade, Sulphate-crosslinked chitosan as an adsorbent for the removal of Congo red dye from aqueous solution, *Air, Soil and Water Research*, 2018, **11**, 117862211881168, doi: 10.1177/1178622118811680.

[28] T. Feng, S. Xiong, F. Zhang, Application of cross-linked porous chitosan films for Congo red adsorption from aqueous solution, *Desalination and Water Treatment*, 2015, **53**, 1970-1976, doi: 10.1080/19443994.2013.870715.

[29] G. Ohemeng-Boahen, D. D. Sewu, H. N. Tran, S. H. Woo, Enhanced adsorption of Congo red from aqueous solution using chitosan/hematite nanocomposite hydrogel capsule fabricated via anionic surfactant gelation, *Colloids and Surfaces A: Physicochemical and Engineering Aspects*, 2021, **625**, 126911, doi: 10.1016/j.colsurfa.2021.126911.

[30] G. A. Kloster, D. Muraca, M. A. Mosiewicki, N. E. Marcovich, Magnetic composite films based on alginate and nano-iron oxide particles obtained by synthesis "in situ", *European Polymer Journal*, 2017, **94**, 43-55, doi: 10.1016/j.eurpolymj.2017.06.041.

[31] W. Zhang, Y. Lan, M. Ma, S. Chai, Q. Zuo, K-H Kim, Y. Gao, A novel chitosan-vanadium-titanium-magnetite composite as a superior adsorbent for organic dyes in wastewater, *Environment International*, 2020, **142**, 105798, doi: 10.1016/j.envint.2020.105798.

[32] S. Chatterjee, G. O.-Boahen, D. D. Sewu, B. A. Osei, S. H. Woo, Improved adsorption of Congo red from aqueous solution using alkali-treated goethite impregnated chitosan hydrogel capsule, *Journal of Environmental Chemical Engineering*, 2022, **10**, 108244, doi: 10.1016/j.jece.2022.108244.

[33] Y. Tan, W. Huang, Q. Lei, S. Huang, K. Yang, X. Chen, D. Li, Insight into the adsorption of magnetic microspheres with large mesopores: tailoring mesoporous structure and ethylenediamine functionalization for ultrahigh Congo red removal, *Separation and Purification Technology*, 2023, **311**, 123265, doi: 10.1016/j.seppur.2023.123265.

[34] E. Zong, R. Fan, H. Hua, J. Yang, S. Jiang, J. Dai, X. Liu, P. Song, A magnetically recyclable lignin-based bio-adsorbent for efficient removal of Congo red from aqueous solution, *International Journal of Biological Macromolecules*, 2023, **226**, 443-453, doi: 10.1016/j.ijbiomac.2022.11.317.

[35] H. Wang, W. Luo, R. Guo, D. Li, B. Xue, Effective adsorption of Congo red dye by magnetic chitosan prepared by solvent-free ball milling, *Materials Chemistry and Physics*, 2022, **292**, 126857, doi: 10.1016/j.matchemphys.2022.126857.

[36] G. Sarojini, S. V. Babu, M. Rajasimman, Adsorptive potential of iron oxide based nanocomposite for the sequestration of Congo red from aqueous solution, *Chemosphere*, 2022, **287**, 132371, doi: 10.1016/j.chemosphere.2021.132371.

[37] L. -Y. Huang, W. Li, N. Du, H. -Q. Lu, L.-D. Meng, K.-Y. Huang, K. Li, Preparation of quaternary ammonium magnetic chitosan microspheres and their application for Congo red adsorption, *Carbohydrate Polymers*, 2022, **297**, 119995, doi: 10.1016/j.carbpol.2022.119995.

[38] R. Massart, E. Dubois, V. Cabuil, E. Hasmonay, Preparation and properties of monodisperse magnetic fluids, *Journal of Magnetism and Magnetic Materials*, 1995, **149**, 1-5, doi: 10.1016/0304-8853(95)00316-9.

[39] G. A. Kloster, M. A. Mosiewicki, N. E. Marcovich, Chitosan/iron oxide nanocomposite films: effect of the composition and preparation methods on the adsorption of Congo red, *Carbohydrate Polymers*, 2019, **221**, 186-194, doi: 10.1016/j.carbpol.2019.05.089.

[40] G. A. Kloster, D. Muraca, O. M. Londoño, M. Knobel, N. E. Marcovich, M. A. Mosiewicki, Structural analysis of magnetic nanocomposites based on chitosan, *Polymer Testing*, 2018, **72**, 202-213, doi: 10.1016/j.polymertesting.2018.10.022.

[41] X. Q. Xu, H. Shen, J. R. Xu, M. Q. Xie, X. J. Li, The colloidal stability and core-shell structure of magnetite nanoparticles coated with alginate, *Applied Surface Science*, 2006, **253**, 2158-2164, doi: 10.1016/j.apsusc.2006.04.015.

[42] D. Pan, S. L. Luo, Y. Feng, X. D. Zhang, F. M. Su, H. Liu, C. T. Liu, X. M. Mai, N. Naik, Z. H. Guo, Highly thermally conductive 3d bn/mwcnts/c spatial network composites with improved electrically insulating and flame retardancy prepared by biological template assisted method. *Composites Part B-Engineering*, 2021, **222**, 109039, doi: 10.1016/j.compositesb.2021.109039.

[43] M. K. Purkait, A. Maiti, S. D. Gupta, S. De, Removal of Congo red using activated carbon and its regeneration, *Journal of Hazardous Materials*, 2007, **145**, 287-295, doi: 10.1016/j.jhazmat.2006.11.021.

[44] H. N. Tran, S-J You, A. H. -Bandegharaei, H. -P. Chao, Mistakes and inconsistencies regarding adsorption of contaminants from aqueous solutions: a critical review, *Water Research*, 2017, **120**, 88-116, doi: 10.1016/j.watres.2017.04.014.

[45] L. Zhang, R. He, H.-C. Gu, Oleic acid coating on the monodisperse magnetite nanoparticles, *Applied Surface Science*, 2006, **253**, 2611-2617, doi: 10.1016/j.apsusc.2006.05.023.

[46] X. Zheng, H. Zheng, Z. Xiong, R. Zhao, Y. Liu, C. Zhao, C. Zheng, Novel anionic polyacrylamide-modify-chitosan magnetic composite nanoparticles with excellent adsorption capacity for cationic dyes and pH-independent adsorption capability for metal ions, *Chemical Engineering Journal*, 2020, **392**, 123706, doi: 10.1016/j.cej.2019.123706.

[47] G. Antarnusa, P. D. Jayanti, Y. R. Denny, A. Suherman, Utilization of co-precipitation method on synthesis of Fe3O4/PEG with different concentrations of PEG for biosensor applications, *Materialia*, 2022, **25**, 101525, doi: 10.1016/j.mtla.2022.101525.

[48] G. A. Kloster, N. E. Marcovich, M. A. Mosiewicki, Composite films based on chitosan and nanomagnetite, *European Polymer Journal*, 2015, **66**, 386-396, doi: 10.1016/j.eurpolymj.2015.02.042.

[49] E. Cheraghipour, M. Pakshir, Process optimization and modeling of Pb(II) ions adsorption on chitosan-conjugated magnetite nano-biocomposite using response surface methodology, *Chemosphere*, 2020, **260**, 127560, doi: 10.1016/j.chemosphere.2020.127560.

[50] L. -Y. Zhang, X.-J. Zhu, H.-W. Sun, G-R. Chi, J.-X. Xu, Y.-L. Sun, Control synthesis of magnetic $Fe_3O_4$-chitosan nanoparticles under UV irradiation in aqueous system, *Current Applied Physics*, 2010, **10**, 828-833, doi: 10.1016/j.cap.2009.10.002.

[51] C. Yuwei, W. Jianlong, Preparation and characterization of magnetic chitosan nanoparticles and its application for Cu(II) removal, *Chemical Engineering Journal*, 2011, **168**, 286-292, doi: 10.1016/j.cej.2011.01.006.

[52] T. E. Khalil, A. F. Elhusseiny, N. M. Ibrahim, A. El-dissouky, Unexpected effect of magnetic nanoparticles on the performance of aqueous removal of toxic Cr(VI) using modified biopolymer chitosan, *International Journal of Biological Macromolecules*, 2021, **170**, 768-779, doi: 10.1016/j.ijbiomac.2020.12.188.

[53] M. R. Robinson, M. Abdelmoula, M. Mallet, R. Coustel, Starch functionalized magnetite nanoparticles: new insight into the structural and magnetic properties, *Journal of Solid State Chemistry*, 2019, **277**, 587-593, doi: 10.1016/j.jssc.2019.06.033.

[54] T. M. Freire, L. M. U. Dutra, D. C. Queiroz, N. M. P. S. Ricardo, K. Barreto, J. C. Denardin, F. R. Wurm, C. P. Sousa, A. N. Correia, P de Lima-Neto, P. B. A. Fechine, Fast ultrasound assisted synthesis of chitosan-based magnetite nanocomposites as a modified electrode sensor, *Carbohydrate Polymers*, 2016, **151**, 760-769, doi: 10.1016/j.carbpol.2016.05.095.

[55] G. Antarnusa, E. Suharyadi, A synthesis of polyethylene glycol (PEG)-coated magnetite Fe3O4 nanoparticles and their characteristics for enhancement of biosensor, *Materials Research Express*, 2020, **7**, 056103, doi: 10.1088/2053-1591/ab8bef.

[56] M. Masuku, L. Ouma, A. Pholosi, Microwave assisted synthesis of oleic acid modified magnetite nanoparticles for benzene adsorption, *Environmental Nanotechnology, Monitoring and Management*, 2021, **15**, 100429, doi: 10.1016/J.ENMM.2021.100429.

[57] J. Li, B. Jiang, Y. Liu, C. Qiu, J. Hu, G. Qian, W. Guo, H. H. Ngo, Preparation and adsorption properties of magnetic chitosan composite adsorbent for $Cu^{2+}$ removal, *Journal of Cleaner Production*, 2017, **158**, 51-58, doi: 10.1016/j.jclepro.2017.04.156.

[58] Poonam, Rana, Apple pectin supported superparamagnetic ($\gamma$-$Fe_2O_3$) maghemite nanoparticles with antimicrobial potency, *Materials Science for Energy Technologies*, 2019, **2**, 15-21, doi: 10.1016/j.mset.2018.09.001.

[59] X. N. Pham, T. P. Nguyen, T. N. Pham, T. T. N. Tran, T. Van Thi Tran, Synthesis and characterization of chitosan-coated magnetite nanoparticles and their application in curcumin drug delivery, *Advances in Natural Sciences: Nanoscience and Nanotechnology*, 2016, **7**, 045010, doi: 10.1088/2043-6262/7/4/045010.

[60] A. Iovescu, G. Stîngă, M. E. Maxim, M. Gosecka, T. Basinska, S. Slomkowski, D. Angelescu, S. Petrescu, N. Stănică, A. Băran, D-F. Anghel, Chitosan-polyglycidol complexes to coating iron oxide particles for dye adsorption, *Carbohydrate Polymers*, 2020, **246**, 116571, doi: 10.1016/j.carbpol.2020.116571.

[61] A. Pawlak, M. Mucha, Thermogravimetric and FTIR studies of chitosan blends, *Thermochimica Acta*, 2003, **396**, 153-166, doi: 10.1016/S0040-6031(02)00523-3.

[62] L. E. Udrea, Preparation and characterization of polyvinyl alcohol-chitosan biocompatible magnetic microparticles, *Journal of Magnetism and Magnetic Materials*, 2011, **323**, 7-13, doi: 10.1016/j.jmmm.2010.06.025.

[63] B. Z. Kurt, F. Uckaya, Z. Durmus, Chitosan and carboxymethyl cellulose based magnetic nanocomposites for application of peroxidase purification, *International Journal of Biological Macromolecules*, 2017, **96**, 149-160, doi: 10.1016/j.ijbiomac.2016.12.042.

[64] P. Sipos, Formation of spherical iron(III) oxyhydroxide nanoparticles sterically stabilized by chitosan in aqueous solutions, *Journal of Inorganic Biochemistry*, 2003, **95**, 55-63, doi: 10.1016/s0162-0134(03)00068-0.

[65] J. Ostrowska-Czubenko, M. Gierszewska-Drużyńska, Effect of ionic crosslinking on the water state in hydrogel chitosan membranes, *Carbohydrate Polymers*, 2009, **77**, 590-598, doi: 10.1016/j.carbpol.2009.01.036.

[66] D. Pan, G. Yang, H. M. Abo-Dief, J. W. Dong, F. M. Su, C. T. Liu, Y. F. Li, B. B. Xu, V. Murugadoss, N. Naik, S. M. El-Bahy, Z. M. El-Bahy, M. A. Huang, Z. H. Guo, Vertically aligned silicon carbide nanowires/ boron nitride cellulose aerogel networks enhanced thermal conductivity and electromagnetic absorbing of epoxy composites, *Nano-Micro Letters*, 2022, **14**, 118, doi: 10.1007/s40820-022-00863-z.

[67] M. Pereda, M. I. Aranguren, N. E. Marcovich, Characterization of chitosan/caseinate films, *Journal of Applied Polymer Science*, 2008, **107**, 1080-1090, doi: 10.1002/app.27052.

[68] J. Wang, M. Mao, S. Atif, Y. Chen, Adsorption behavior and mechanism of aqueous Cr(III) and Cr(III)-EDTA chelates on DTPA-chitosan modified $Fe_3O_4@SiO_2$, *Reactive and Functional Polymers*, 2020, **156**, 104720, doi: 10.1016/j.reactfunctpolym.2020.104720.

[69] S. F. Wang, L. Shen, Y. J. Tong, L. Chen, I. Y. Phang, P. Q. Lim, T. X. Liu, Biopolymer chitosan/montmorillonite nanocomposites: preparation and characterization, *Polymer Degradation and Stability*, 2005, **90**, 123-131, doi: 10.1016/j.polymdegradstab.2005.03.001.

[70] M. Lavorgna, F. Piscitelli, P. Mangiacapra, G. G. Buonocore, Study of the combined effect of both clay and glycerol plasticizer on the properties of chitosan films, *Carbohydrate Polymers*, 2010, **82**, 291-298, doi: 10.1016/j.carbpol.2010.04.054.

[71] M. A. Abdelaziz, M. E. Owda, R. E. Abouzeid, O. Alaysuy, E. I. Mohamed, Kinetics, isotherms, and mechanism of removing cationic and anionic dyes from aqueous solutions using chitosan/magnetite/silver nanoparticles, *International Journal of Biological Macromolecules*, 2023, **225**, 1462-1475, doi: 10.1016/j.ijbiomac.2022.11.203.

[72] V. Karthika, M. S. AlSalhi, S. Devanesan, K. Gopinath, A. Arumugam, M. Govindarajan, Chitosan overlaid $Fe_3O_4$/rGO

nanocomposite for targeted drug delivery, imaging, and biomedical applications, *Scientific Reports*, 2020, **10**, 18912, doi: 10.1038/s41598-020-76015-3.

[73] J. M. Coey, Magnetism and magnetic materials, Cambridge university press, 2010.

[74] J. L. Dormann, D. Fiorani, E. Tronc, Magnetic relaxation in fine-particle systems. Advances in Chemical Physics. Hoboken, NJ, USA: John Wiley & Sons, Inc., 2007, 283-494, doi: 10.1002/9780470141571.ch4.

[75] F. Fabris, K.-H. Tu, C. A. Ross, W. C. Nunes, Influence of dipolar interactions on the magnetic properties of superparamagnetic particle systems, *Journal of Applied Physics*, 2019, **126**, 173905, doi: 10.1063/1.5125595.

[76] I. Khmara, O. Strbak, V. Zavisova, M. Koneracka, M. Kubovcikova, I. Antal, V. Kavecansky, D. Lucanska, D. Dobrota, P. Kopcansky, Chitosan-stabilized iron oxide nanoparticles for magnetic resonance imaging, *Journal of Magnetism and Magnetic Materials*, 2019, **474**, 319-325, doi: 10.1016/j.jmmm.2018.11.026.

[77] A. Zhu, L. Yuan, T. Liao, Suspension of Fe3O4 nanoparticles stabilized by chitosan and o-carboxymethylchitosan, *International Journal of Pharmaceutics*, 2008, **350**, 361-368, doi: 10.1016/j.ijpharm.2007.09.004.

[78] R. M. Patil, P. B. Shete, N. D. Thorat, S. V. Otari, K. C. Barick, A. Prasad, R. S. Ningthoujam, B. M. Tiwale, S. H. Pawar, Superparamagnetic iron oxide/chitosan core/shells for hyperthermia application: improved colloidal stability and biocompatibility, *Journal of Magnetism and Magnetic Materials*, 2014, **355**, 22-30, doi: 10.1016/j.jmmm.2013.11.033.

[79] C. G. Malar, M. Seenuvasan, K. S. Kumar, Improvisation of diffusion coefficient in surface modified magnetite nanoparticles: a novel perspective, *Materials Science and Engineering: C*, 2019, **103**, 109832, doi: 10.1016/j.msec.2019.109832.

[80] M. Saini, R. Gupta, Fabrication of chitosan-coated magnetite nanobiocatalyst with Bacillus atrophaeus γ-glutamyl transpeptidase and its application to the synthesis of a bioactive peptide SCV-07, *Process Biochemistry*, 2022, **122**, 238-249, doi: 10.1016/j.procbio.2022.08.034.

[81] P. Arévalo-Cid, J. Isasi, A. C. Caballero, F. Martín-Hernández, R. González-Rubio, Effects of shell-thickness on the powder morphology, magnetic behavior and stability of the chitosan-coated $Fe_3O_4$ nanoparticles, Boletín De La Sociedad Española De Cerámica y Vidrio, 2022, **61**, 300-312, doi: 10.1016/j.bsecv.2020.12.001.

[82] V. Zamora-Mora, M. Fernández-Gutiérrez, J. S. Román, G. Goya, R. Hernández, C. Mijangos, Magnetic core-shell chitosan nanoparticles: Rheological characterization and hyperthermia application, *Carbohydrate Polymers*, 2014, **102**, 691-698, doi: 10.1016/j.carbpol.2013.10.101.

[83] K. Saravanakumar, A. Sathiyaseelan, P. Manivasagan, M. S. Jeong, M. Choi, E.-S. Jang, V. V. Priya, M.-H. Wang, Photothermally responsive chitosan-coated iron oxide nanoparticles for enhanced eradication of bacterial biofilms, *Biomaterials Advances*, 2022, **141**, 213129, doi: 10.1016/j.bioadv.2022.213129.

[84] W. Zhang, Nanoparticle aggregation: principles and modeling, *Advances in experimental medicine and biology*, Dordrecht: Springer Netherlands, 2014, 19-43, doi: 10.1007/978-94-017-8739-0_2.

[85] A. E. Regazzoni, G. A. Urrutia, M. A. Blesa, A. J. G. Maroto, Some observations on the composition and morphology of synthetic magnetites obtained by different routes, *Journal of Inorganic and Nuclear Chemistry*, 1981, **43**, 1489-1493, doi: 10.1016/0022-1902(81)80322-3.

[86] G. A. Kloster, M. Valiente, N. E. Marcovich, M. A. Mosiewicki, Adsorption of arsenic onto films based on chitosan and chitosan/nano-iron oxide, *International Journal of Biological Macromolecules*, 2020, **165**, 1286-1295, doi: 10.1016/j.ijbiomac.2020.09.244.

[87] H. Jonassen, A.-L. Kjøniksen, M. Hiorth, Stability of chitosan nanoparticles cross-linked with tripolyphosphate, *Biomacromolecules*, 2012, **13**, 3747-3756, doi: 10.1021/bm301207a.

[88] C. Mansour, G. Lefèvre, E. M. Pavageau, H. Catalette, M. Fédoroff, S. Zanna, Sorption of sulfate ions onto magnetite, *Journal of Colloid and Interface Science*, 2009, **331**, 77-82, doi: 10.1016/j.jcis.2008.11.009.

[89] G. L. Dotto, J. M. Moura, T. R. S. Cadaval, L. A. A. Pinto, Application of chitosan films for the removal of food dyes from aqueous solutions by adsorption, *Chemical Engineering Journal*, 2013, **214**, 8-16, doi: 10.1016/j.cej.2012.10.027.

[90] A. K. Sharma, Priya, B. S. Kaith, N. Sharma, J. K. Bhatia, V. Tanwar, S. Panchal, S. Bajaj, Selective removal of cationic dyes using response surface methodology optimized gum acacia-sodium alginate blended superadsorbent, *International Journal of Biological Macromolecules*, 2019, **124**, 331-345, doi: 10.1016/j.ijbiomac.2018.11.213.

[91] Y. Xu, J. Bao, X. Zhang, W. Li, Y. Xie, S. Sun, W. Zhao, C. Zhao, Functionalized polyethersulfone nanofibrous membranes with ultra-high adsorption capacity for organic dyes by one-step electrospinning, *Journal of Colloid And Interface Science*, 2019, **533**, 526-538.

[92] T. R. Sahoo, B. Prelot, Adsorption processes for the removal of contaminants from wastewater: the perspective role of nanomaterials and nanotechnology, *Nanomaterials for the Detection and Removal of Wastewater Pollutants*, 2020, 161-222.

[93] J. A. González, M. Villanueva, L. Piehl, G. Copello, Development of a chitin/graphene oxide hybrid composite for the removal of pollutant dyes: Adsorption and desorption study, *Chemical Engineering Journal*, 2015, **280**, 41-48, doi: 10.1016/J.CEJ.2015.05.112.

[94] J. N. Wekoye, W. C. Wanyonyi, P. T. Wangila, M. K. Tonui, Kinetic and equilibrium studies of Congo red dye adsorption on cabbage waste powder, *Environmental Chemistry and Ecotoxicology*, 2020, **2**, 24-31, doi: 10.1016/j.enceco.2020.01.004.

[95] H. Zhu, M. Zhang, Y. Liu, L. Zhang, R. Han, Study of Congo red adsorption onto chitosan coated magnetic iron oxide in batch mode, *Desalination and Water Treatment*, 2012, **37**, 46-54, doi: 10.1080/19443994.2012.661252.

[96] S. Chatterjee, S. Chatterjee, B. P. Chatterjee, A. K. Guha, Adsorptive removal of Congo red, a carcinogenic textile dye by chitosan hydrobeads: binding mechanism, equilibrium and kinetics, *Colloids and Surfaces A: Physicochemical and Engineering Aspects*, 2007, **299**, 146-152, doi: 10.1016/j.colsurfa.2006.11.036.

[97] X. Zheng, X. Li, J. Li, L. Wang, W. Jin, J. liu, Y. Pei, K. Tang, Efficient removal of anionic dye (Congo red) by dialdehyde microfibrillated cellulose/chitosan composite film with significantly improved stability in dye solution, *International Journal of Biological Macromolecules*, 2018, **107**, 283-289.

[98] Z. Khan, S. A. Al-Thabaiti, Chitosan capped trimetallic nanoparticles: synthesis and their Congo red adsorbing activities, *International Journal of Biological Macromolecules*, 2022, **194**, 580-593, doi: 10.1016/j.ijbiomac.2021.11.101.

[99] Z. U. Ahmad, L. Yao. J. Wang, D. D. Gang, F. Islam, Q. Lian, M. E. Zappi, Neodymium embedded ordered mesoporous carbon (OMC) for enhanced adsorption of sunset yellow: Characterizations, adsorption study and adsorption mechanism, *Chemical Engineering Journal*, 2019, **359**, 814-826, doi: 10.1016/j.cej.2018.11.174.

[100] L. Chao, Y. Wang, S. Chen, Y. Li, Preparation and adsorption properties of chitosan-modified magnetic nanoparticles for removal of Mo (VI) ions, *Polish Journal of Environmental Studies*, 2021, **30**, 2489-2498, doi: 10.15244/pjoes/130039.

[101] J. Wen, Y. Fang, G. Zeng, Progress and prospect of adsorptive removal of heavy metal ions from aqueous solution using metal-organic frameworks: a review of studies from the last decade, *Chemosphere*, 2018, **201**, 627-643, doi: 10.1016/j.chemosphere.2018.03.047.

[102] M. A. Rafiee, J. Rafiee, Z. Wang, H. Song, Z.-Z. Yu, N. Koratkar, Enhanced mechanical properties of nanocomposites at low graphene content, *ACS Nano*, 2009, **3**, 3884-3890, doi: 10.1021/nn9010472.

[103] W. S. Hummers Jr, R. E. Offeman, Preparation of graphitic oxide, *Journal of the American Chemical Society*, 1958, **80**, 1339, doi: 10.1021/ja01539a017.

[104] H. Demiral, L. Demiral, F. Tümsek, B. Karabacakoğlu, Adsorption of chromium(VI) from aqueous solution by activated carbon derived from olive bagasse and applicability of different adsorption models, *Chemical Engineering Journal*, 2008, **144**, 188-196, doi: 10.1016/j.cej.2008.01.020.

[105] E. Asgari, A. Sheikhmohammadi, J. Yeganeh, Application of the Fe3O4-chitosan nano-adsorbent for the adsorption of metronidazole from wastewater: Optimization, kinetic, thermodynamic and equilibrium studies, *International Journal of Biological Macromolecules*, 2020, **164**, 694-706, doi: 10.1016/j.ijbiomac.2020.07.188.

[106] T. K. Barman, M. Pandya, T. Mathur, T. Bhadauriya, M. Rao, S. Khan, S. Singhal, P. Bhateja, R. Sood, S. Malhotra, B. Das, J. Paliwal, P. K. Bhatnagar, D. J. Upadhyay, Novel biaryl oxazolidinones: in vitro and in vivo activities with pharmacokinetics in an animal model, *International Journal of Antimicrobial Agents*, 2009, **33**, 280-284, doi: 10.1016/j.ijantimicag.2008.08.025.

[107] H. N. Tran, Improper estimation of thermodynamic parameters in adsorption studies with distribution coefficient KD (qe/Ce) or freundlich constant (KF): considerations from the derivation of dimensionless thermodynamic equilibrium constant and suggestions, *Adsorption Science & Technology*, 2022, **2022**, 1-23, doi: 10.1155/2022/5553212.

[108] H. Hemond, L. Fechner, Preface. Chemical Fate and Transport in the Environment. Amsterdam: Elsevier, 2015: ix-x, doi: 10.1016/b978-0-12-398256-8.09988-6.

[109] A. Fenti, P. Iovino, S. Salvestrini, Some remarks on “a critical review of the estimation of the thermodynamic parameters on adsorption equilibria. Wrong use of equilibrium constant in the Van't Hoof equation for calculation of thermodynamic parameters of adsorption, *Journal of Molecular Liquids*, 2019, **276**, 529-530, doi: 10.1016/j.molliq.2018.12.019.

[110] K. K. Singh, M. Talat, S. H. Hasan, Removal of lead from aqueous solutions by agricultural waste maize bran, *Bioresource Technology*, 2006, **97**, 2124-2130, doi: 10.1016/j.biortech.2005.09.016.

[111] E. Kumar, A. Bhatnagar, M. Ji, W. Jung, S. -H. Lee, S. -J. Kim, G. Lee, H. Song, J.-Y. Choi, J. -S. Yang, B. -H. Jeon, Defluoridation from aqueous solutions by granular ferric hydroxide (GFH), *Water Research*, 2009, **43**, 490-498, doi: 10.1016/j.watres.2008.10.031.

[112] Amir, Mokhtari, 3D porous bioadsorbents based on chitosan/alginate/cellulose nanofibers as efficient and recyclable adsorbents of anionic dye, *Carbohydrate Polymers*, 2021, **265**, 118075, doi: 10.1016/j.carbpol.2021.118075.